ELSEVIER

Catalysis Today 58 (2000) 167–197

CATALYSIS TODAY

www.elsevier.com/locate/cattod

Reaction engineering of suspended solid heterogeneous photocatalytic reactors

Alberto E. Cassano* (Professor), Orlando M. Alfano (Professor)

Instituto de Desarrollo Tecnológico para la Industria Química, Universidad Nacional del Litoral and CONICET, Güemes 3450, 3000 Santa Fe, Argentina

Abstract

A revision of the authors' work on suspended solid photocatalytic reactors is presented. Thus, heterogeneous reactions in aqueous media, involving the presence of both fine particles of titanium dioxide and UV radiation are analyzed. Under these conditions, light scattering is a complex phenomenon that must be included in the description of the system performance. Suspended solid photocatalytic reactors are just a family of the well-known slurry reactors for which considerable progress has been reported in the reaction engineering literature. However, ab initio design methods for these particular — light activated — reactors are not known. Previous developed methods should be readily applicable if: (1) the photocatalytic activation is properly described, (2) an intrinsic kinetic expression can be developed, and (3) the scalar field of radiation intensities inside reaction spaces of different geometries can also be known. With this purpose, in order to model the radiation field and also the initiation step, the radiative transfer equation (RTE) for heterogeneous media must be solved. Solution of the RTE in photocatalytic reactors implies the knowledge of different system properties that are not usually known. New methods for obtaining this information are described and typical results are presented. Scale up procedures, derived from the application of first principles, cannot be applied if intrinsic reaction kinetic data are not available. A key point in developing these reaction rate expressions is the knowledge of the radiation absorption by the catalytic particles. The required model is also presented. Furthermore, a simple reactor design and special operating conditions for appropriate laboratory experiments were developed that can be used to produce this type of data reducing to a minimum the difficulties associated with the analysis of composition vs. time information. In this review, the photocatalytic oxidation of trichloroethylene is used as a model reaction. Finally, the description of the radiation field distribution in a typical flat plate, photocatalytic solar reactor simulator illustrates the method that should be used for scaling-up purposes. With this objective the photon absorption rate was obtained as a function of position and the developed model was verified with careful experimental measurements.

Keywords: Photocatalytic reactors; Suspended solid; Titanium dioxide; Reaction kinetics; Light absorption; Light scattering; Reaction engineering

Nomenclature

ABS	absorbance measurement (dimensionless)
a_S	particle surface area (cm^2 per particle)
a_V	solid–liquid interfacial area per unit reactor volume ($cm^2\,cm^{-3}$)
C_A	geometric (radiation) concentration factor (dimensionless)
C_i	molar concentration of component i ($mol\,cm^{-3}$)

* Corresponding author. Tel.: +54-342-4559175; fax: +54-342-4559185.
E-mail address: acassano@alpha.arcride.edu.ar (A.E. Cassano)

0920-5861/00/$ – see front matter
PII: S0920-5861(00)00251-0

C_{mp}	mass catalyst concentration (g cm^{-3})
d	spectrophotometer cell thickness (cm)
e^a	volumetric rate of (radiation) energy absorption (Einstein s^{-1} cm^{-3})
$e^a(\underline{x}, t)\|_P$	rate of (radiation) energy absorption per particle (Einstein s^{-1} per particle)
E	a function defined in Eq. (22) (dimensionless)
f	a function of the stated variables and parameters
G	incident radiation (also known as spherical irradiance) (Einstein s^{-1} cm^{-2})
h	thickness of the planar reactor (cm)
H	depth (cm)
I	specific (radiation) intensity (also known as radiance) (Einstein s^{-1} cm^{-2} sr^{-1})
j^e	radiation emission (Einstein s^{-1} cm^{-3} sr^{-1})
$\underline{J}_i$	molar diffusive density flux vector of component i (mol s^{-1} cm^{-2})
k	kinetic constant (for different reaction steps) (varies with step)
K	adsorption equilibrium constant (cm^3 mol^{-1})
L	length (cm)
LVREA	local volumetric rate of (radiation) energy absorption (Einstein s^{-1} cm^{-3})
$\underline{n}$	unit normal vector
N	number of particles
N_V	number of particles per unit volume (particles cm^{-3})
p	phase function (dimensionless)
P	output power from the lamp (Einstein s^{-1})
q	radiation density flux for a given direction or surface orientation (also known as superficial irradiance) (Einstein s^{-1} cm^{-2})
$\underline{q}$	radiation density flux vector (Einstein s^{-1} cm^{-2})
r	radius (cm)
r_g	rate of electron–hole generation per particle (mol s^{-1} per particle)
r_P	reaction rate per particle (mol s^{-1} per particle)
r_S	superficial reaction rate (mol s^{-1} cm^{-2})
r_{Susp}	reaction rate per unit suspension volume (mol s^{-1} cm^{-3})
s	variable representing distances in a 3D space (cm)
S_g	catalyst surface area (cm^2 g^{-1})
t	time (s)
V	volume (cm^3)
VREA	some average of the LVREA (Einstein s^{-1} cm^{-3})
v_P	particle volume (cm^3 per particle)
x	Cartesian coordinate (cm)
$\underline{x}$	vector representing position in a 3D space (cm)
y	Cartesian coordinate (cm)
z	Cartesian coordinate (cm)

Greek letters

$\alpha'_1 = \alpha^*_1$	defined by Eq. (22) (mol s^{-1}per particle)
$\alpha'_{3,i} = \alpha^*_{3,i}$	defined by Eqs. (23) and (43) (cm^3 mol^{-1})
$\alpha'_{3,j}$	defined by Eq. (23) (cm^3 mol^{-1})
α^*_2	defined by Eq. (31) (g s Einstein^{-1})
β	cylindrical coordinate (rad)
β	extinction coefficient=$\kappa+\sigma$ (cm^{-1})
γ	fraction of absorbed photons from incident radiation (dimensionless)
Γ	reflection or compounded reflection coefficient (dimensionless)
δ	wall thickness (cm)
Λ	ratio of direct to diffuse solar radiation fluxes (dimensionless)
ε	liquid hold-up (dimensionless)
$\underline{\zeta}$	3D position vector inside a material particle (cm)
η	direction cosine $\eta=\sin\theta\cos\phi$
$\eta_{d,i}$	reaction collection efficiency (dimensionless)
η_E	energy collection efficiency (dimensionless)
η_q	radiation density flux collection efficiency (dimensionless)
θ	spherical coordinate (rad)
κ	absorption coefficient (cm^{-1})
κ^*	specific (per unit mass) absorption coefficient (cm^2 g^{-1})
λ	wavelength (nm=10^{-7} cm)
μ	direction cosine $\mu=\cos\theta$

ρ_P	particle density ($g\,cm^{-3}$)
ρ	interfacial reflectivity (dimensionless)
σ	scattering coefficient (cm^{-1})
σ^*	specific (per unit mass) scattering coefficient ($cm^2\,g^{-1}$)
τ	glass internal transmittance (dimensionless)
τ	catalyst collection efficiency: Eq. (74) (dimensionless)
Y	transmission or compounded transmission coefficient (dimensionless)
ϕ	spherical coordinate (rad)
ϕ_a	activation quantum yield (mol $Einstein^{-1}$)
Ω	solid angle (sr, ster radian)
$\underline{\Omega}$	unit vector in the direction of radiation propagation
Ω_0	angle between two directions of propagation (rad)

Superscripts

a	denotes absorbed energy
DIFF	denotes diffuse radiation from the sun
DIR	denotes direct radiation from the sun
Dir	denotes direct radiation from the lamp
Ref	denotes reflected radiation from the reflector
*	denotes specific (per unit mass) properties

Subscripts

A	denotes area
BK	denotes back direction
FR	denotes forward direction
in, IN	denotes solid angle of incoming radiation
L	denotes liquid phase
M	means modified value
0	denotes initial value or inlet condition
P	denotes particle
R	denotes reactor
S	denotes solid phase
S	denotes superficial value
Sol	denotes solid surface
Susp	denotes suspension
t	denotes thickness
T	denotes total
Tk	denotes tank
V	denotes volume
λ	denotes wavelength
Σ	denotes polychromatic radiation
$\underline{\Omega}$	denotes direction of radiation propagation

Special symbols

_	denotes vector value
[]	denotes concentration
$\langle\rangle$	denotes average value
$\bar{}$	denotes average over wavelengths

1. Introduction

Photocatalytic reactions constitute one of the emerging technologies for chemical transformations of different kinds. In the late 1970s, the initial stages of their development were boosted by very attractive proposals concerning water splitting using solar UV energy. Developed expectations were not fulfilled and in the early 1980s, when the enthusiasm was fading out, a new potential application was rising in the horizon because it was found that photocatalytic reactions could have an important impact providing new technologies for processes of environmental remediation. Notwithstanding that several investigations in organic synthesis have been reported, the abatement of air and water pollution remains as the most important target for applications and the main driving force for research and development studies.

Several compounds have been investigated as potential catalysts. However, considering: (1) chemical activity, (2) stability under different operating conditions, (3) availability and handiness in many physical forms, (4) cost, and (5) lack of toxicity, the most widely used catalyst is titanium dioxide.

Photocatalytic reactions are the result of the interaction of photons having the appropriate wavelength (i.e., energy) with a semiconductor. When the arriving light has an energy equal or greater than the semiconductor band gap, radiation is absorbed and electrons are moved from the valence band to the conduction band giving rise to the formation of electron–hole pairs. These charge carriers can migrate to the catalyst surface in competition with an exothermic and

normally fast recombination reaction. When they reach the semiconductor surface they may, once more recombine, or participate in successive oxidation and reduction reactions. Thus, activation of the catalyst is the photochemical act, while — leaving aside parallel photolysis — subsequent dark reactions lead to the degradation of many water and air pollutants. If and when the oxidative–reductive reactions are fully completed, organic substances, e.g., are totally mineralized and transformed into water, carbon dioxide and a mineral acid (when other elements besides carbon, hydrogen and oxygen are present).

These reactions are very attractive for treating pollution problems because a wide range of contaminants may be fully destroyed and the resulting products are just cleaner air or water streams and the recovered catalyst. Many different compounds have been investigated (including some specific reactions with inorganic substances), and with a whole spectrum of rates, the vast majority of them can be completely mineralized.

Different types of reactors can be used for photocatalytic reactions. Table 1 shows a short summary of the possibilities. Fig. 1 shows some reactors that can be used for water detoxification employing artificial UV light. For treating air pollution, monoliths coated with titanium dioxide (Fig. 2) and thin films of the catalysts immobilized on usually flat walls have been the preferred choice. The latter, was frequently applied on the tiles covering the walls of different rooms usually illuminated with normal fluorescent tubes.

Table 1
Heterogeneous photocatalytic reactors

Gas–solid systems	Monoliths[b]
	Packed beds[c]
	Catalytic walls[b]
	Fluidized beds
Liquid–solid systems	Well-stirred slurries[b]
	Fluidized beds[c]
	Packed beds[c]
	Catalytic walls[a,b]
Gas–liquid–solid systems	Trickle beds
	Packed bubble columns
	Well-stirred slurries[c]
	Bubble column slurries[c]
	Fluidized beds
	Moving beds

[a] Include membrane and fiber optic reactors.
[b] Most commonly used as photocatalytic reactors.
[c] Less widely used as photocatalytic reactors.
All other reactors are much less (or not) reported in the photocatalytic literature.

One of the most attractive features of photocatalytic reactions comes from the possibility of using

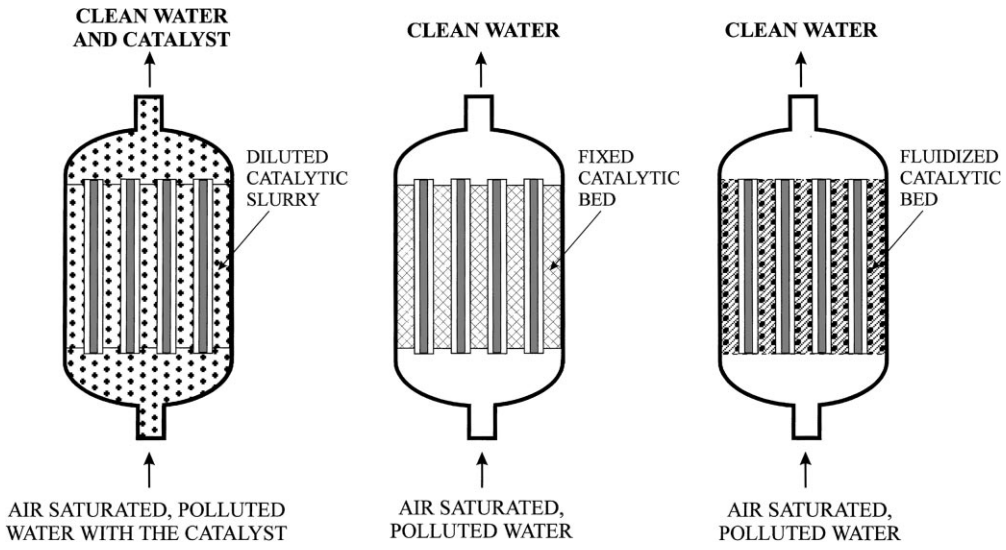

Fig. 1. Photocatalytic reactors for liquid phase applications employing artificial light. Left: slurry reactor; center: Packed-bed reactor; right: Fluidized-bed reactor.

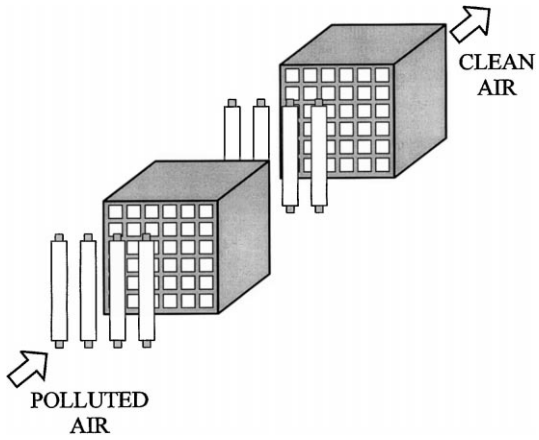

Fig. 2. Monolith reactors for gas phase applications.

solar energy. Unfortunately, not more than 3–4% of the solar flux arriving to the earth surface is useful for activating unmodified titanium dioxide (absorption starts at 380/390 nm, but is becoming significant only below 350/360 nm). However, in different configurations, solar reactors have been used in several pilot plant studies for water detoxification. Fig. 3 shows some typical reactors that have been operated at the Plataforma Solar de Almeria (Spain) and the Institute for Solar Energy (ISFH) in Hannover (Germany).

Most of the published work in water environments tends to coincide that the slurry system made of fine semiconductor particles exhibit the largest catalytic activity as compared with equivalent loading for an immobilized catalyst. It is also recognized, however, that the suspended catalyst operation presents the drawback of (normally) requiring additional costs for separating the catalytic particles from the treated water stream. Nevertheless, considering all the different reactor systems that can and/or have been used in photocatalytic reactions and particularly in the liquid phase, employing both artificial or solar irradiation, the well stirred suspended solid (slurry) reactor has been the most widely used.

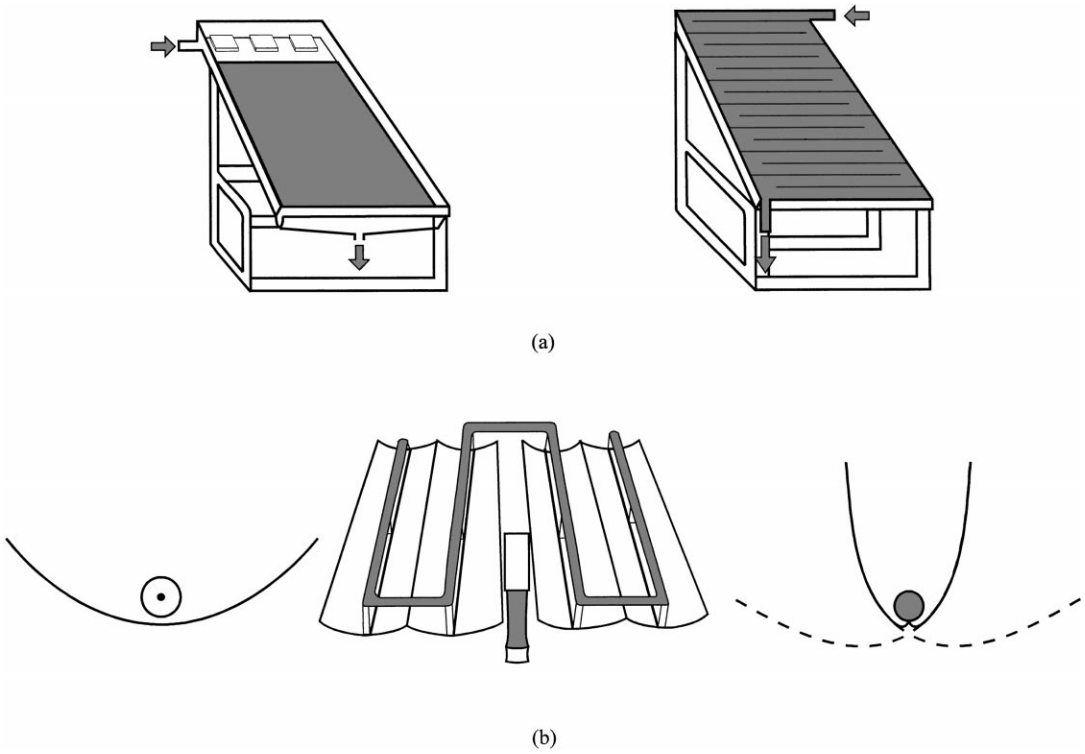

Fig. 3. Photocatalytic reactors for liquid phase applications employing solar light. (a) Reactors used at ISFH in Hannover; left: Thin film, fixed-bed reactor; right: Plexiglas, double-skin-sheet reactor. (b) Reactors used at Plataforma Solar de Almería (Spain); left: geometry of the parabolic collector; center: parabolic trough reactor; right: geometry of the compound parabolic collector.

Many and very important contributions have been reported concerning the chemical feasibility of these reactions. Considerable progress has also been made in the understanding of some reaction mechanisms and/or pathways. No parallel effort has been observed in the engineering aspects of these processes; particularly in the proposal of design and scaling-up procedures aimed at bypassing costly and time consuming sequences of empirical steps when laboratory results are to be transformed into practical applications.

This review paper presents our contributions to the understanding of the performance of slurry photocatalytic reactors. We are founding our approach on the fundamentals of chemical engineering science. Starting from first principles, and using mathematical modeling as a main tool, we have progressed in our knowledge of these reactors supporting our developments with careful experimental verification of all the newly introduced concepts. The final objective is to develop design procedures that, in principle, should allow to design practical photocatalytic reactors employing laboratory experiments exclusively.

2. Reactor design (the distinctive problem of photocatalytic reactions)

Most — if not all — of the reactor types that can be adopted for photocatalytic reactions have already been used for thermal or thermal-catalytic reactions and are fairly well known in the chemical engineering literature. This means that if we could have reliable and intrinsic reaction kinetics for a particular application we could, in principle, proceed with the design and scale-up of the process. However, photocatalytic reactions, as any other photochemical reaction, have a very distinctive characteristic: the reaction is activated by light absorption, and consequently, the radiation distribution in both, the laboratory reactor where the reaction kinetics must be obtained, and that corresponding to the large-scale application, must be known. Fig. 4 gives an illustration of the problem at stake. Starting with the objective — a design problem — we immediately face a first difference: when considering light propagation, the geometry of the reactor is much more important than in thermal reactors. Radiation transport considerations (meaningful absorption distances, view factors between energy source and reactor walls, etc.) as well as pre-established shapes and sizes of the different radiation sources — even when using solar energy — place important limitations to the designer choices. Restrictions are even more severe with titanium dioxide because it has strong radiation absorption properties below 350 nm and for usual catalyst concentrations, <10 mm of the reaction space turn the reactor totally opaque.

Having decided on the geometry, as usual when writing mass balances, we need an intrinsic reaction

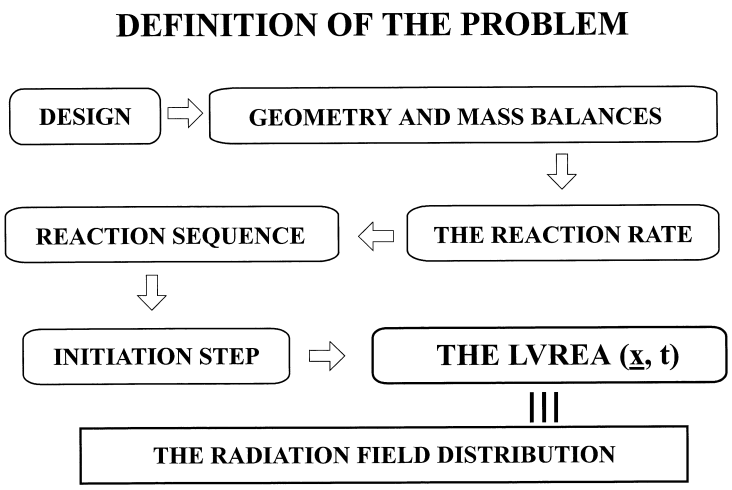

Fig. 4. The photocatalytic reactor design sequence showing the distinctive problem in light activated reactions.

rate — independent of the reactor shape and configuration. Under the best conditions, this reaction rate will be obtained with the appropriate laboratory experiments, from a known reaction sequence — or even better, when available, a reaction mechanism. They always include a light activated step. The intrinsic description of this first step will necessarily call for the knowledge of the radiation field inside the experimental reactor. Even for phenomenological expressions — kinetics rates not derived from reaction sequences or mechanisms — the radiation distribution must be known. In any event, once the initiation step — the rate of electron–hole generation — is known it can be incorporated into the reaction kinetic model and afterwards the different reaction parameters obtained with experiments.

When the reaction rate is known, to carry out the reactor design we must resort to the classical momentum, energy — if thermal effects resulting from the reaction were important — and mass balances. However, for the large-scale photocatalytic reactor a usually independent radiation transport balance will be required. This means that in both cases, the performance description of the laboratory reactor and that of the large-scale reactor, will always require the knowledge of the local — and sometimes time-dependent — photon absorption rate, or more properly designated, the local volumetric rate of energy absorption (the LVREA).

If: (1) the intrinsic reaction kinetics is known, (2) a group of the most suitable (or probable) lamps has been chosen, (3) the tentative shape of the reactor has been decided and (4) the radiation distribution in the adopted reactor geometry is also known, then the reactor design can be obtained by a straightforward extension of already developed methods for thermal catalytic reactors. Hence, for both, the intrinsic kinetics studies and the reactor scale-up and design, the LVREA is the key and distinctive property to be known. It can be obtained from the solution of the radiative transfer equation.

3. Fundamental equations for radiation transport

From the radiation transport point of view, slurry photocatalytic reactors employing a suspension of fine solid particles are very different than homogeneous photochemical systems because radiation scattering cannot be neglected. When scattering is present the well-known Lambert–Beer equation does not apply and one needs to describe the radiation field with the complete radiative transfer equation. The rigorous form of the radiation transport equation (RTE) applied to photochemical reactors was originally published by Spadoni et al. [1]. A more detailed presentation can be found in [2].

For monochromatic light and assuming that: (1) steady state has been achieved (the radiation field is established at the speed of the light), (2) scattering is independent (valid for the usual concentrations employed in photocatalysis), (3) scattering is elastic, i.e., scattering changes only the direction of the flying photons (also valid for the usual semiconductor particles employed in photocatalysis), and (4) scattering is multiple, the radiation transport can be represented by

$$\frac{\mathrm{d}I_{\lambda,\underline{\Omega}}(s,t)}{\mathrm{d}s} + \underbrace{\kappa_\lambda(s,t)I_{\lambda,\underline{\Omega}}(s,t)}_{\text{absorption}} + \underbrace{\sigma_\lambda(s,t)I_{\lambda,\underline{\Omega}}(s,t)}_{\text{out-scattering}} = \underbrace{j^{\mathrm{e}}_\lambda(s,t)}_{\text{emission}} + \frac{\sigma_\lambda(s,t)}{4\pi} \times \underbrace{\int_{\Omega'=4\pi} p(\underline{\Omega}' \to \underline{\Omega}) I_{\lambda,\underline{\Omega}'}(s,t)\,\mathrm{d}\Omega'}_{\text{in-scattering}} \quad (1)$$

Thus, the radiation at a point $s(\underline{x})$ in space, having a given direction of propagation $\underline{\Omega}$, traveling along distances measured by the spatial parameter "s", may be changed by: (1) a gain of photons by emission (normally neglected inside photocatalytic reaction spaces, unless very high temperatures are employed), (2) a loss of photons by absorption, (3) a loss of photons by out-scattering, and (4) a gain of photons by in-scattering resulting from multiple scattering phenomena occurring in the space surrounding point $s(\underline{x})$. Note that this equation is written in terms of the spectral specific intensity (also known as spectral radiance). This is always required when radiation is not a collimated beam of parallel rays. The time dependence of the radiation intensities may be the result of time-dependent radiation field properties. Since scattering is independent, the volumetric absorption and scattering coefficients bear a linear relationship with the catalyst concentration. The phase function for scattering distribution, the function "p", accounts for the existence of multiple scattering, giving rise

to the in-scattering phenomenon that incorporates photons (I_λ) coming from any arbitrary direction $\underline{\Omega}'$ into the adopted direction for writing the RTE ($\underline{\Omega}$). The presence of this particular term gives to the RTE its integro-differential nature and is responsible for most of the difficulties associated with its numerical integration.

If the spatial spectral specific intensity distribution is known $\{I[s(\underline{x}), \underline{\Omega}(\theta, \phi), t]\}$, three properties can be immediately derived:

1. The incident radiation:

$$G_\lambda(\underline{x}, t) = \int_\Omega I_{\lambda,\underline{\Omega}}(\underline{x}, t)\, \mathrm{d}\Omega \tag{2}$$

   where the integration on directions is performed over the solid angle corresponding to all radiation rays trajectories arriving at point $s(\underline{x})$.
2. The local volumetric rate of energy absorption (LVREA):

$$e^{\mathrm{a}}_\lambda(\underline{x}, t) = \kappa_\lambda(\underline{x}, t) \int_\Omega I_{\lambda,\underline{\Omega}}(\underline{x}, t)\, \mathrm{d}\Omega \tag{3}$$

   Employing polychromatic light the LVREA results:

$$e^{\mathrm{a}}(\underline{x}, t) = \int_\lambda \mathrm{d}\lambda\, \kappa_\lambda(\underline{x}, t) \int_\Omega I_{\lambda,\underline{\Omega}}(\underline{x}, t)\, \mathrm{d}\Omega \tag{4}$$

3. The radiation density flux vector:

$$\underline{q}_\lambda(\underline{x}, t) = \int_\Omega I_\lambda(\underline{x}, \underline{\Omega}, t)\underline{\Omega}\, \mathrm{d}\Omega \tag{5}$$

Under kinetically controlled regimes, the rate of electron–hole generation is always proportional to the LVREA. In the photocatalytic reaction space, the spatial distribution of polychromatic light absorption is fully described by the scalar field of the $e^{\mathrm{a}}_{\Sigma\lambda}(\underline{x}, t)$ values. To simplify matters, if the radiation field is independent of time (that means constant optical properties of the catalysts and steady illumination in the macroscopic time scale), values of the LVREA can be obtained if the spatial $s[(\underline{x})]$ and directional $[\underline{\Omega}(\theta, \phi)]$ distributions of the specific intensities are known. For this reason the solution of the RTE is the first, almost unavoidable step, to arrive at intrinsic kinetic parameters.

4. Evaluation of the LVREA

As mentioned before, to develop the reaction kinetics we must know the LVREA. The existence of strong absorption and scattering makes this evaluation more difficult because: (1) the reaction space has an irreducible, strong spatial non-uniformity, (2) absorption and scattering are inseparable phenomena, (3) homogeneous actinometry cannot be used, (4) there is scarce information regarding the optical properties of the catalyst, (5) there is no good information about the type of phase function to be used for representing the spatial distribution of the scattering produced by titanium dioxide, (6) the solution of the complete RTE is not simple, and (7) does not exist a good model for describing radiation absorption by a material point (in the continuous mechanics definition) of the catalytic suspension. Most of the steps that one must follow to get the photon absorption rate in an experimental laboratory reactor are also required for describing the radiation field in a large-scale reactor. Then, for both objectives, the following problems must be solved:

1. Formulate the RTE for the chosen geometry.
2. Measure the absorption and scattering coefficient.
3. Measure or select the phase function.
4. Solve the RTE for that particular geometric configuration.
5. Calculate photon absorption rates by the solid particles of the suspension.

It will be seen in the next sections that to obtain the results indicated in 2, we also need those of points 3 and 4. Hence, an iterative procedure must be applied.

4.1. Formulate the RTE

The solution of the RTE is facilitated if Cartesian geometry is used. Let us begin with this problem. Brandi et al. [3] developed a two-dimensional ((*x*,*y*) in space) — two directional ((θ,φ) in the propagating directions) mathematical model. According to Fig. 5:

$$\mu\frac{\partial I_{\lambda,\underline{\Omega}}}{\partial x} + \eta\frac{\partial I_{\lambda,\underline{\Omega}}}{\partial y} = -(\kappa_\lambda + \sigma_\lambda) I_{\lambda,\underline{\Omega}} + \frac{\sigma_\lambda}{4\pi}\int_{\underline{\Omega}'} p(\underline{\Omega}' \to \underline{\Omega}) I_{\lambda,\underline{\Omega}'}(x, y)\, \mathrm{d}\Omega' \tag{6}$$

where $\mu = \cos\theta$ and $\eta = \sin\theta\cos\phi$ (direction cosines of the propagating trajectory with respect to the *x* and

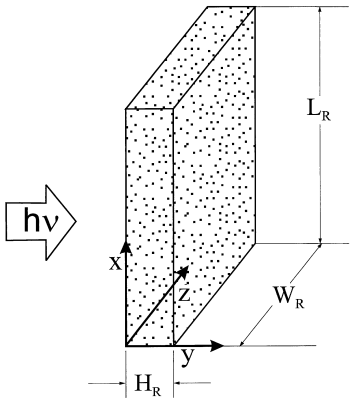

Fig. 5. The flat plate geometry for photocatalytic reactors.

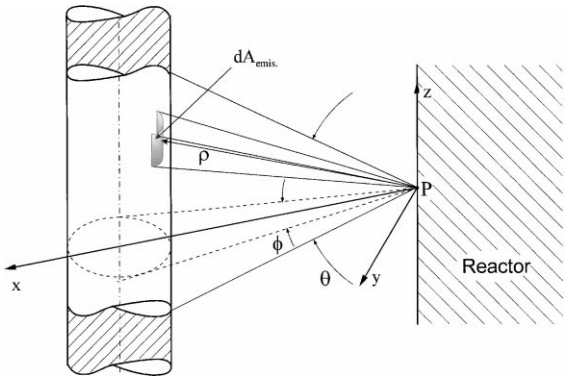

Fig. 6. Geometry for the modeling of radiation emission from a tubular lamp. Adapted from Cassano et al. [2].

y coordinates, respectively). The following boundary conditions were used:

$$I_{\lambda,\underline{\Omega}}(x, y = 0, \ \underline{\Omega} = \underline{\Omega}_{IN}) = \Im \text{ (radiation emitting system and reactor wall properties)} \quad (6a)$$

$$I_{\lambda,\underline{\Omega}}(x, y = H_R, \ \underline{\Omega} = \underline{\Omega}_{IN}) = I_{\lambda,\underline{\Omega}}(x = 0, y, \underline{\Omega} = \underline{\Omega}_{IN}) = I_{\lambda,\underline{\Omega}}(x = L_R, y, \underline{\Omega} = \underline{\Omega}_{IN}) = 0 \quad (6b)$$

The BC (Eq. (6a)) can be obtained from an emission model representing radiation arriving at a point of space, generated by all emitters existing in the volume or the surface of the radiation source [4]. The emission model permits to calculate at any point $P(\underline{x})$ in space, irradiated by a given lamp, all the radiation contributions received from each one of the elementary emitters existing in the lamp volume that can be seen from the given point $P(\underline{x})$ under analysis (Fig. 6). If emission is produced by the lamp surface, the model considers elementary surface emitters [2]. Then, from a given lamp, radiation intensities at any point on the reactor surface facing the lamp can be precisely calculated. All the needed information is: (1) full description of the output power from the lamp, (2) the lamp geometrical dimensions, and (3) the distances from the lamp to the surface [2]. If the emission is accomplished with the aid of reflectors, more complex emission models are also available [5–8].

The same authors [9] in order to incorporate more realistic boundary conditions later perfected this model. Then, at $y=0$

$$I_{M,\lambda}(x, y = 0, \underline{\Omega}_{IN}) = Y_{W,\lambda}(\underline{\Omega})$$
$$I_{0,\lambda}(x, y = 0 - \delta, \underline{\Omega}_{IN}) + \Gamma_{SGA,\lambda}(\underline{\Omega})$$
$$I_{BK,\lambda}(x, y = 0, \underline{\Omega}_{BK}) \quad (7)$$

The new BC incorporates the most important properties of the reactor wall (reflection at both interfaces and internal absorption inside the wall thickness). With this purpose, the BC at the internal side of the reactor wall was obtained by direct application of the net radiation method [10]. In Eq. (7), δ is the wall thickness, $I_{0,\lambda}$ is the result produced by the emission model at the external boundary of the reactor wall ($y=0-\delta$), $I_{BK,\lambda}$ is the intensity corresponding to back scattering at the internal boundary of the reactor wall, and $Y_{w,\lambda}$ and $\Gamma_{SGA,\lambda}$ are complex functions of the reflectivities at both interfaces (gas–glass and glass–water) and the internal transmission of the glass wall. The existence of $I_{BK,\lambda}$ makes necessary to solve the integro-differential equation with an iterative method. More details on this model will be presented in a section ahead.

At the opposite face of the rectangular space ($y=H_R$), the boundary condition must account for a reflecting boundary but with no radiation coming from outside. Once more, the net radiation method was used to account for reflection at both interfaces and absorption at the wall.

$$I_{M,\lambda}(x, y = H_R, \underline{\Omega}_{IN}) = \Gamma_{SGA,\lambda}(\underline{\Omega})$$
$$I_{FR,\lambda}(x, y = H_R, \underline{\Omega}_{OU}) \quad (8)$$

In Eq. (8) $I_{FR,\lambda}$ is the intensity escaping from the reaction space at $y=H_R$ and $\Gamma_{SGA,\lambda}$ is once more the

complex function of the reflectivities at both interfaces and the internal transmission of the glass wall. For the boundaries at $x=0$ and $x=L_R$ non-reflecting, non-emitting surfaces were assumed. Again, $I_{FR,\lambda}$ must be obtained by iteration.

4.2. Absorption and scattering coefficients

Unfortunately, there is no direct experimental method available to obtain separate values of the absorption and scattering coefficients. Two independent measurements are needed; they must recognize that absorption and scattering are inseparable phenomena. We have devised an iterative method that can provide a good answer to the problem. Iteration is necessary because our method is based on the application of the RTE to the cells of a spectrophotometer and some of its accessories and a trial-and-error approach cannot be avoided. This is so because we have not yet selected the best phase function for scattering, consequently, initially, several phase functions must be used in parallel. A short description is presented below based on our original proposal [11].

We have proposed the following independent measurements: (1) collimated transmittance measurements (Fig. 7a), in the normal absorption mode and maximizing out-scattering losses in the radiation detector (placing the sample cell as far as possible from it) and (2) diffuse transmittance measurements (Fig. 7b), with the integrating sphere of a diffuse reflectance accessory, and collecting in the detector all transmitted photons in the forward direction.

In the first type of measurement, since out scattering is maximized, we get a measurement of the total extinction coefficient:

$$\beta_\lambda(C_{mp}) = \kappa_\lambda(C_{mp}) + \sigma_\lambda(C_{mp}) \tag{9}$$

Experiments with an almost unidirectional sample beam, from 290 to 410 nm were performed at different catalyst concentrations within the linear range of the extinction vs. concentration plots (one for each wavelength). With a linear regression program, enforcing a zero intercept, the specific (per unit mass concentration) extinction coefficient was obtained.

$$\beta^*_\lambda = \frac{\beta_\lambda}{C_{mp}} \tag{10}$$

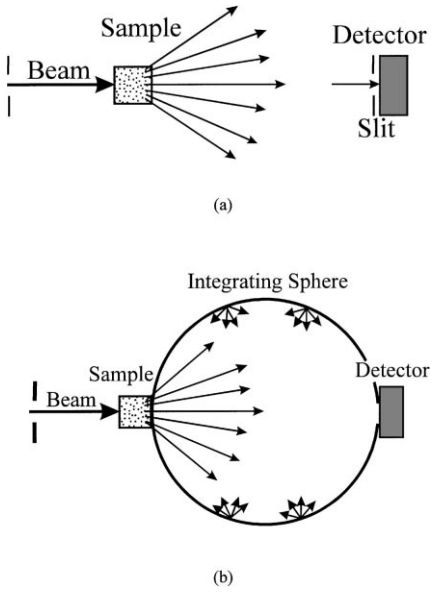

Fig. 7. Experimental determination of absorption and scattering coefficients. (a) Collimated transmittance; (b) diffuse transmittance. Adapted from Cabrera et al. [11].

Knowing β^*_λ, if we could know either κ^*_λ or σ^*_λ we can calculate the other by a simple subtraction. In the second set of experiments, the detector collects all the non-absorbed and forwardly scattered photons. It can be shown [11] that the absorbance reading in the spectrophotometer detector are equal to the ratio of two radiation fluxes, the one in the denominator corresponding to the reference beam, according to:

$$ABS_\lambda = -\log_{10}\frac{q^+_\lambda(x=d)}{q^+_\lambda(x=0)} \tag{11}$$

This measurement is not enough to have a complete set of two independent equations to be solved for κ^*_λ and σ^*_λ. This is so, because the integrating sphere and the detector have not collected all the out-scattered rays. At this point, if we had a rigorous mathematical model representing the behavior of the sample cell, we could estimate both the non-absorbed photons and the forwardly scattered photons. Comparing the theoretically predicted readings with the experimental measurements, and resorting to an optimization program for parameter estimation, we could get either κ_λ or σ_λ. Since these values can be obtained as a function of the catalyst concentration, the specific absorption or scattering coefficients could be readily calculated:

$$\sigma_\lambda^* = \frac{\sigma_\lambda}{C_{\mathrm{mp}}} \ (\mathrm{cm}^2\,\mathrm{g}^{-1}) \ \text{and} \ (\kappa_\lambda^* = \beta_\lambda^* - \sigma_\lambda^*) \qquad (12)$$

Therefore, we need the model representing radiation transport in the sample cell and the solution of the RTE for this particular geometrical configuration. The flat plate model is a very convenient representation for the flat plate characteristics of the spectrophotometric cells. For the sample cell the problem is somehow simpler because the ratio defined in Eq. (11) makes unnecessary to know the absolute value of the incoming radiation flux (the absolute value of the incoming intensity for both beams, at x=0, cancels out). Additionally, in the particular case of the spectrophotometer radiation source, only a few directions of incidence must be taken into account because the instrument optics produces an almost unidirectional irradiation.

We must keep in mind that, even if we could guess some values for both optical parameters, we still do not know the phase function to be used. Here the first loop of a trial and error procedure begins.

4.3. Selection of a phase function

The next problem that one encounters to solve Eq. (6) is the selection of a good phase function model for representing scattering by titanium dioxide. The in-scattering term of the RTE asks for it. Experimental measurements are very difficult, particularly for the complexity of the equipment that should be used. An alternate approach is to select a theoretical model from the available proposals in the radiation transport theory. The simplest model considers that scattering is isotropic. Then the phase function can be represented by

$$p(\underline{\Omega}' \rightarrow \underline{\Omega}) = 1 \qquad (13)$$

Two more models for scattering are also frequently described in the literature (see Fig. 8). The specular reflection model can hardly be considered a good approximation for titanium dioxide. On the other hand, the diffuse reflectance phase function model could be a thinkable choice:

$$p[\Omega_0(\theta, \phi)] = \frac{8}{3\pi}(\sin\Omega_0 - \Omega_0 \cos\Omega_0) \qquad (14)$$

As it will be explained further along the paper (experimental verification of the radiation field model for a flat plate reactor) it was possible to show that the best results were provided by the isotropic phase function. However, until that result could be obtained, in all our evaluations, we worked with both models. Iteration was also needed here because the optical parameters are also used to decide, with the aid of the flat plate reactor, on the best phase function model. Since estimation of the optical parameters needed a phase function, this part of the method constitutes the second loop in our trial-and-error procedure.

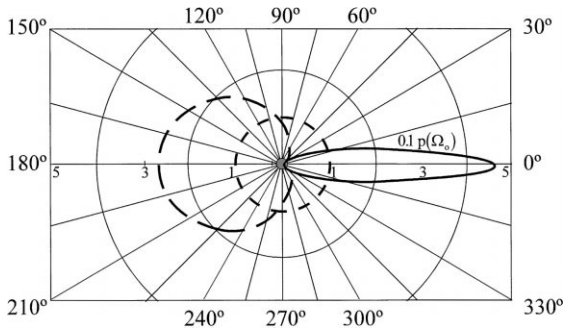

Fig. 8. Models of phase functions for scattering. The sharp figure to the right represents the specular reflection model; the lobe to the left the diffuse reflection model. Reproduced from [22]. Copyright 1995 with permission from American Chemical Society.

4.4. Solution of the RTE

The RTE is an integro-differential equation that has no simple solution. Let us recall that specific intensities are described with the following variables: $I = I[\underline{x}(x, y), \underline{\Omega}(\mu, \eta), \lambda, t]$. Hence, we need two variables for position in space, two for the propagating direction, plus wavelength and time. For some simple geometries, and working with isotropic scattering, some analytical solutions are possible. This type of transport equation has similar mathematical features than the models that are used to describe neutron transport. A powerful numerical method of solution has been obtained for this application within the frame of the generalized transport theory that can be adapted for photon transport. It is called the discrete ordinate method [12]. The method transforms Eq. (6) into a complex system of algebraic equations that can be solved with a computer. A brief description of the numerical method can be found in our work [13]. In

this paper the solution was developed for a cylindrical geometry (an annular reactor) where numerical difficulties are more severe. At this point suffices to say that, in general, and assuming steady state conditions and constant physical properties [$I_\lambda \neq I_\lambda(t)$], three separate discretizations are needed: (1) a spatial discretization (in x and y) for each wavelength and each direction, that can be obtained employing central finite differences, (2) a directional discretization (in μ and η), at each point in space and for each wavelength (in this case, a specific Set of Directions (S_n), having specially defined geometrical characteristics must be defined; in our case each octant was expanded with 36 directions (S_n=16) with good success), and finally (3) a spectral (in wavelengths) discretization to account for polychromatic irradiation having divided the wavelength range in 12 equally spaced intervals (290–410 nm).

At this point we can go back to the optical properties evaluation. As we already know, from collimated transmittance measurements the RTE can be written in terms of β_λ and σ_λ. Solving Eq. (6), for the sample cell we could predict light transmitted in the forward direction from the cell to the integrating sphere. However, we must recall that when doing so, we still have one unknown left, because we only know the value of the extinction coefficient (β_λ). An optimization program for parameter estimation can be used to compare numerical predictions of the forward fluxes with experimental measurements in the integrating sphere of the spectrophotometer diffuse reflectance accessory, rendering the best value of the scattering coefficient as a function of wavelength. From the β_λ and σ_λ values, the absorption coefficient is obtained by difference. Fig. 9 shows some typical results for different commercial brands of titanium dioxide. Samples were prepared according to a prescribed protocol in order to reproduce the suspension physical properties.

These calculations for the optical properties can be carried out for different phase functions. Iteration between these calculations and those experiments devised to decide on the best phase function (a section further below), will render — when both trial-and-error procedures are completed — the set of absorption and scattering coefficients and the best phase function for titanium dioxide.

It must be specially remarked that the solution of the RTE using this method for estimating the optical parameters will render values of specific intensities (and consequently the LVREA) for the whole suspension. In other words, the liquid and the solid could be radiation-absorbing species. However, absorption by the liquid can be easily evaluated by standard and very conventional measurements. The evaluation of the radiation absorbed by the solid is treated in the next section.

4.5. Light absorption rate by the solid particles of a catalytic suspension

In a previous paper [14], we developed the concepts of this model. In the continuum mechanics sense, a material point in space is a volume for which every property can be well defined by a single value (e.g., temperature, density, concentration, etc.). Its size may be very large if the system is uniform and at equilibrium or very small if significant gradients are present. For a catalytic suspension, it will be made of the liquid and the solid phases. Let us consider a small volume V_{TOT} of the suspension space. This volume is located at a point in space $\underline{\mathrm{x}}$ (Fig. 10). Any point inside V_{TOT} can be defined in terms of a local reference frame $\underline{\varsigma}$. The particles of most of the known varieties of titanium dioxide have a non-porous structure; then, absorption of radiation is produced in the particle volume through its bounding surface that is characterized by a unit normal vector $\underline{n}_{\mathrm{s}}$, pointing outwards. Let us assume that geometric optics applies ($\lambda <$particle size). At a given point on the surface, radiation arrives from different directions in the surrounding space. This energy defines a vector of radiation flux [15] at point P, given by

$$\underline{\mathrm{q}}_\lambda(\underline{\mathrm{x}}+\underline{\zeta}_{\mathrm{p}},t)=\int_{\Omega=4\pi} I_\lambda(\underline{\mathrm{x}}+\underline{\zeta}_{\mathrm{p}},t,\underline{\Omega})\underline{\Omega}\,\mathrm{d}\Omega \qquad (15)$$

Part of this radiation may be reflected and part will be absorbed. The flux that is going inside the particle and is absorbed is

$$\begin{aligned}\mathrm{d}e^{\mathrm{a}}_\lambda(\underline{\mathrm{x}}+\underline{\zeta}_{\mathrm{p}},t)&=[\underline{\mathrm{q}}_\lambda(\underline{\mathrm{x}}+\underline{\zeta}_{\mathrm{p}},t)\cdot\underline{\mathrm{n}}_{\mathrm{L}}]\mathrm{d}A\\&=\left[\int_{\Omega=4\pi} I_\lambda(\underline{\mathrm{x}}+\underline{\zeta}_{\mathrm{p}},t,\underline{\Omega})\underline{\Omega}\cdot\underline{\mathrm{n}}_L\,\mathrm{d}\Omega\right]\mathrm{d}A \qquad (16)\end{aligned}$$

for all positive values of the dot product.

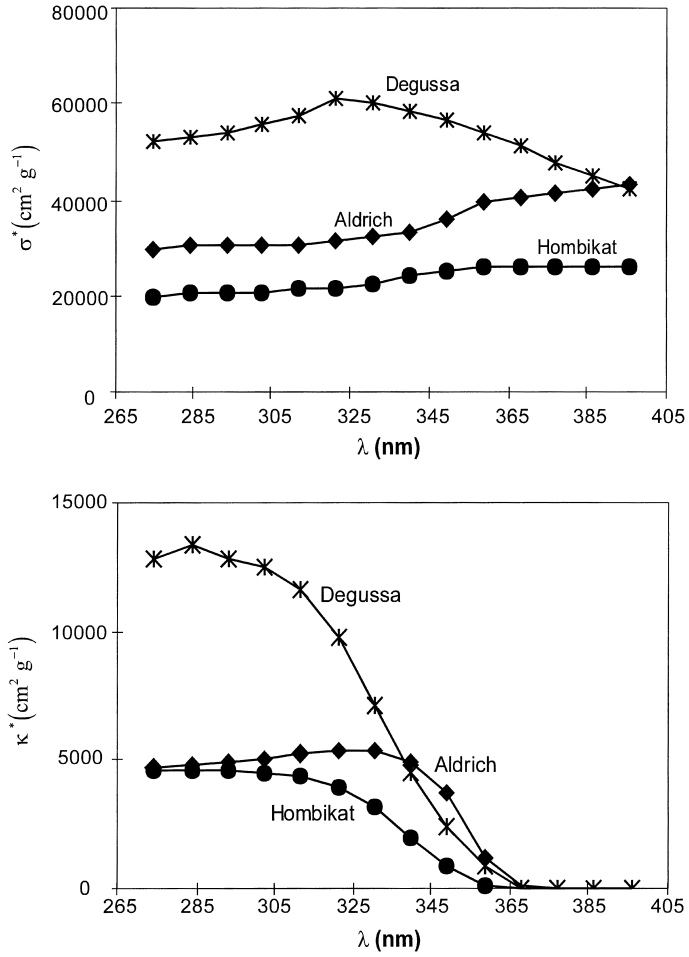

Fig. 9. Absorption and scattering coefficients of different brands of titanium dioxide. Reproduced from [11]. Copyright 1996 with permission from American Chemical Society.

Using the methodology described by the same authors [14], the value of the LVREA per material point of suspension (liquid plus solid) is

$$e^{a}_{\lambda}(\underline{x}, t) = \varepsilon_{L} \left\langle e^{a}_{\lambda,L}(\underline{x} + \underline{\zeta}, t) \right\rangle_{V_L} + N_V \int_{V_{Sol,P}} dV\, e^{a}_{\lambda,Sol}(\underline{x} + \underline{\zeta}, t) \quad (17)$$

where it has been assumed that all particles have equal volume and that $N_V = N/V_{TOT}$ is the number of particles per unit volume.

The value of the LVREA by a single, solid particle is

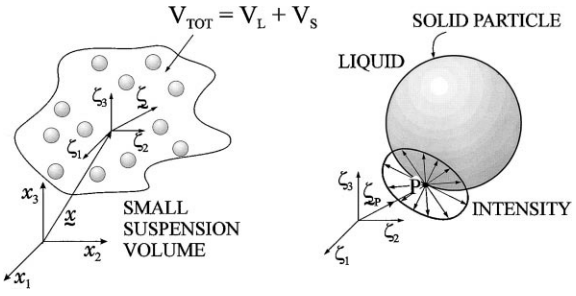

Fig. 10. Modeling of radiation absorption by the solid phase of a catalytic suspension. Adapted from Alfano et al. [14].

$$e^{a}_{\Sigma\lambda,\mathrm{Sol}}(\underline{x},t)|_{P} = \frac{1}{N_V}\int_{\lambda_1}^{\lambda_2} d\lambda \times \left[e^{a}_{\lambda}(\underline{x},t) - \varepsilon_L \left\langle e^{a}_{\lambda,L}(\underline{x}+\underline{\zeta},t)\right\rangle_{V_L}\right] \quad (18)$$

If the liquid is transparent, we get

$$e^{a}_{\Sigma\lambda,\mathrm{Sol}}(\underline{x},t)|_{P} = \frac{1}{N_V}\int_{\lambda_1}^{\lambda_2} d\lambda\, e^{a}_{\lambda}(\underline{x},t) \quad (19)$$

If the liquid is not transparent and the pollutant produces absorption, the LVREA by the liquid must be used to formulate the initiation step of the parallel homogeneous reaction. In any event, when absorption by the liquid phase is present, both absorbents produce attenuation of radiation inside the reactor: the liquid and the solid. Attenuation is due to both phenomena but each one of them defines a different activation step. Activation of the solid is the only one that is needed to formulate the photocatalytic initiation step.

5. Gathering intrinsic kinetic information

Knowing how to calculate the LVREA we can now proceed to obtain valid kinetic information in the laboratory reactor. Our present knowledge will be valid if our experimental reactor retains the flat plate configuration. If not, additional effort will be necessary to integrate the RTE in a different geometry. Nonetheless, our information regarding the optical parameters and the phase function will be valid regardless the reactor configuration. Values of $e^{a}(\underline{x},t)$ must be known or calculated for (1) each type of catalyst, (2) the different catalyst concentrations (including catalyst agglomeration and/or catalyst aging), (3) the experimental reactor geometry, and (4) the characteristics of the employed illumination (that defines the incident radiation on the reactor window for radiation entrance). Let us look at our proposed way to obtain the reaction kinetics for the degradation of a model compound. If we maintain the Cartesian geometry and further assume steady state operation of the catalyst, the following problems must be solved:

1. Adoption or proposal of a kinetic scheme.
2. Development of the kinetic model.
3. Description of the rate of electron–hole generation.
4. Evaluation of the LVREA in the experimental reactor. The laboratory reactor radiation model.
5. Interpretation of the heterogeneous reaction rate. The laboratory reactor mass balance model.

5.1. Kinetic scheme

This is one of the most difficult problems. Well-established and accepted reaction mechanisms for photocatalytic reactions, even for simple model compounds, are very scarce. It seems that a general reaction mechanism, even for the oxidative or the reductive paths separately will not be possible. Then, we must resort to plausible reaction sequences and sometimes nothing more than very simple phenomenological equations. Even if these rather simpler problems could be satisfactorily solved, one must keep in mind that the proposal of a working kinetic equation will be much more involved when complex reaction mixtures of real wastewaters are to be studied (sometimes involving variable composition with time). Knowing these limitations, let us begin by considering the following reacting system:

- The catalyst is a suspension (in water) of fine particles of titanium dioxide.
- The substrate is a hydrocarbon compound amenable of hydroxyl radical attack (on the carbon–hydrogen bond).
- The catalyst activating energy is radiation in the near UV range: $300<\lambda<400$ nm. The lower limit defined by the practical (glass) transmission of the reactor window and the upper one by the titanium dioxide absorption.
- Oxygen is always present in excess in the reacting medium (to simplify the reaction sequence).
- There is no parallel homogeneous reaction (the model compound does not absorb radiation in the working wavelength range).
- The catalyst surface remains unchanged during the reaction.
- Mixing conditions are such that there are no mass transport limitations (either for the reactant or for oxygen).

For the kinetic scheme (Table 2) we adopt a reaction sequence proposed by Turchi and Ollis [16] that includes the following steps: (1) catalyst activation by radiation, (2) adsorption of water, the organic compound and the generated hydroxyl radical on the

Table 2
Reaction scheme[a]

Activation	$TiO_2 \rightarrow^{h\nu} e^- + h^+$	(1)
Adsorption		
	$O_L^{2-} + Ti^{IV} + H_2O \leftrightarrow O_L H^- + Ti^{IV}–OH^-$	(2a)
	$Ti^{IV} + H_2O \leftrightarrow Ti^{IV}–H_2O$	(2b)
	$site + R_i \leftrightarrow R_{i,ads}$	(3)
	$OH^\bullet + Ti^{IV} \leftrightarrow Ti^{IV}\|OH^\bullet$	(4)
Recombination		
	$e^- + h^+ \rightarrow heat$	(5)
Hole trapping		
	$Ti^{IV}–OH^- + h^+ \leftrightarrow Ti^{IV}\|OH^\bullet$	(6a)
	$Ti^{IV}–H_2O + h^+ \leftrightarrow Ti^{IV}\|OH^\bullet + H^+$	(6b)
	$R_{i,ads} + h^+ \leftrightarrow R_{i,ads}^+$	(7)
Electron trapping		
	$Ti^{IV} + e^- \leftrightarrow Ti^{III}$	(8a)
	$Ti^{III} + O_2 \leftrightarrow Ti^{IV}–O_2^-$	(8b)
Hydroxyl attack		
Case I	$Ti^{IV}\|OH^\bullet + R_{i,ads} \rightarrow Ti^{IV} + R_{j,ads}$	(9)
Case II	$OH^\bullet + R_{i,ads} \rightarrow R_{j,ads}$	(10)
Case III	$Ti^{IV}\|OH^\bullet + R_i \rightarrow Ti^{IV} + R_j$	(11)
Case IV	$OH^\bullet + R_i \rightarrow R_j$	(12)

[a] Extracted from Turchi and Ollis [16].

catalytic surface, (3) recombination of electrons and holes, (4) hole trapping by the adsorbed species, (5) electron trapping, having oxygen as the main electron acceptor, (6) $OH^\bullet$ radical attack on the substrate R_i, and (7) reaction of the $OH^\bullet$ radical with different compounds [R_j (j=1, 2, …, n; $j \neq i$], including reaction products or intermediates (j=$k \cdots n$).

For our proposed methodology, any other kinetic scheme could be equally suitable, including more complicated mechanisms. For modeling trichloroethylene degradation — our chosen model compound — the previous sequence may be sufficient. The method can be equally applied to any other form of a more complete reaction sequence. Among them, e.g., subsequent reactions derived from the interaction of oxygen with electrons and/or effect of the oxygen concentration. The key points of the method are: (1) define the initiation reaction, (2) define the termination reaction, and (3) define the most significant path for pollutant degradation. The method, as it is now, cannot include reaction inhibitions (anions and cations) as well as catalyst poisoning.

5.2. Reaction kinetic model

The following assumptions have been used: (1) direct hole oxidation is not an important hole trapping reaction, (2) all adsorption processes on the catalytic surface are in equilibrium, (3) the steady state approximation applies to hydroxyl radicals and semiconductor holes, (4) the concentration of hydroxyl ions and water on the catalytic surface is constant, (5) recombination of electrons and holes is assumed to occur in the bulk of the catalytic particle; the model can be easily expanded to include recombination at the catalytic surface, (6) the concentration of electrons and holes are equal, and (7) the rate of electron and holes generation can be defined.

The first six are a subset of Turchi and Ollis implicit or explicit assumptions. Under these conditions, the following reaction rate per catalytic particle can be derived [14]:

$$r_P(\underline{x}, t) = \alpha_1' \frac{\alpha_{3,i}[R_i]}{1 + E(R_i, R_j)} \left\{ - \frac{E(R_i, R_j)}{1 + E(R_i, R_j)} + \left(\left\{ \frac{E(R_i, R_j)}{1 + E(R_i, R_j)} \right\}^2 + \frac{2}{\alpha_1'} r_g \right)^{1/2} \right\} \quad (20)$$

In Eq. (20), the rate of electrons and holes (e–h) generation is defined as

$$r_g(\underline{x}) = \int_{\lambda_1}^{\lambda} d\lambda \, \phi_{a,\lambda} e_\lambda^a(\underline{x}) \quad (21)$$

Obviously a function of the catalyst concentration that affects the radiation field and of the irradiation rate arriving to the reactor.

In Eq. (21) an activation quantum yield for e–h generation in a non-ideal semiconductor has been used. Note that the kinetics parameters included in Eq. (20) are a combination of kinetic constants and adsorption equilibrium constants defined in the reaction scheme described in Table 2. For example:

$$\alpha_1' = \frac{(k_{6+}' a_S)^2}{2 k_5 v_p},$$

$$E(R_i, R_{j \neq i}) = \alpha_{3,i}[R_i] + \sum_{j=1, j \neq i}^{n} a_{3,j}[R_j] \quad (22)$$

$$\begin{aligned} \alpha_{3,i} &= f_i(k_{6-}, k_9, k_{10}, k_{11}, k_{12}, K_{3,i}, K_4, a_s, [Ti^{IV}] \text{ and } [site]) \\ \alpha_{3,j} &= f_j(k_{6-}, k_{Rj,I}, k_{Rj,II}, k_{Rj,III}, k_{Rj,IV}, K_{3,j}, K_4, a_s, [Ti^{IV}] \text{ and } [site]) \end{aligned} \quad (23)$$

The kinetic expression [Eqs. (20) and (21)] has all the special features that have been already found in photocatalytic systems. It can be easily shown that if

$$\left\{\frac{E(R_i, R_j)}{1 + E(R_i, R_j)}\right\}^2 \gg \frac{2}{\alpha_1'} r_g \tag{24}$$

$$\begin{aligned} r_p &\cong \text{const.}_I \times f_I(R_i, R_j) \times r_g \\ &\cong \text{const.}_I^* \times f_I(R_i, R_j) \times e^a_{\Sigma\lambda}(\underline{x}) \end{aligned} \tag{25}$$

which says that when the rate of electron–hole generation is smaller than a given value (that depends on the chemical system under consideration), the reaction rate bears a linear dependence with the photon absorption rate, because the rate of electron–hole generation is proportional to the LVREA [Eq. (21)]. When

$$\left\{\frac{E(R_i, R_j)}{1 + E(R_i, R_j)}\right\}^2 \ll \frac{2}{\alpha_1'} r_g \tag{26}$$

$$\begin{aligned} r_p &\cong \text{const.}_{II} \times f_{II}(R_i, R_j) \times \sqrt{r_g} \\ &\cong \text{const.}_{II}^* \times f_{II}(R_i, R_j) \times \sqrt{e^a_{\Sigma\lambda}(\underline{x})} \end{aligned} \tag{27}$$

which indicates that when the rate of electron–hole generation is larger than the above-described term, the reaction rate exhibits square root dependence with respect to the absorbed energy.

These two limiting conditions have been frequently reported in the literature. Notice that the zero-order dependence with respect to the LVREA cannot be obtained if the reaction is kinetically controlled, a situation that has been explicitly included in our proposed reacting system. What is more important is that the photon absorption rate is usually a strong function of position, and due to the high radiation absorption normally encountered in photocatalytic systems, both kinetic regimes may coexist inside the same reactor (including a transition sub-regime between them).

5.3. Rate of electron–hole generation

Combining Eq. (19) with Eq. (21) for a steady state catalyst:

$$\begin{aligned} r_g(\underline{x}) &= \int_{\lambda_1}^{\lambda_2} d\lambda\, \phi_{a,\lambda} e^a_\lambda(\underline{x}, \underline{\zeta}_p) \Big|_p \\ &= \frac{1}{N_V} \int_{\lambda_1}^{\lambda_2} d\lambda\, \phi_{a,\lambda} e^a_\lambda(\underline{x}) \end{aligned} \tag{28}$$

This means that if we can solve the RTE in our experimental reactor and get the values of $I_\lambda(\underline{x}, \underline{\Omega})$ as a function of wavelength, position and direction, we can calculate the LVREA according to Eqs. (3) and (4) and obtain the value of r_g. It may be convenient to define an average value (over wavelengths) for the activation quantum yield according to

$$\bar{\phi}_a = \frac{\int_\lambda d\lambda\, \phi_{a,\lambda}\ e^a_\lambda}{\int_\lambda d\lambda\ e^a_\lambda} \tag{29}$$

Finally

$$\begin{aligned} r_P = \alpha_1^* \left\{\frac{\alpha^*_{3,i}[R_i]}{1 + E(R_i, R_j)}\right\} \Bigg\{ &- \frac{E(R_i, R_j)}{1 + E(R_i, R_j)} \\ &+ \left(\left\{\frac{E(R_i, R_j)}{1 + E(R_i, R_j)}\right\}^2 \right. \\ &\left. + \frac{\alpha_2^*}{C_{mp}} \int_{\lambda_1}^{\lambda_2} d\lambda\, e^a_\lambda[\underline{x}, (C_{mp})] \right)^{1/2} \Bigg\} \end{aligned} \tag{30}$$

with

$$\begin{aligned} &\alpha_1^* = \alpha_1'; \qquad N_V = \frac{C_{mp}}{v_p \rho_p}; \\ &\alpha_2^* = \frac{2 v_p \rho_p \bar{\phi}_a}{\alpha_1'} \ \text{ and } \ \alpha^*_{3,i} = \alpha'_{3,i} \end{aligned} \tag{31}$$

5.4. Evaluation of the LVREA in the experimental reactor (the laboratory reactor radiation model)

At this point we are in the position of making our decision regarding the experimental reactor to be used. Cabrera et al. [17] proposed a new experimental reactor that — with a few changes — has been successfully used for kinetic studies in our group. Fig. 11 gives a schematic description of the device. It is made of the following parts:

1. A cylindrical reactor with two flat windows made of good quality Pyrex glass. If needed these two windows may be made of Suprasil quality quartz. The window for radiation entrance has its external face made with ground glass. The reactor has an optical

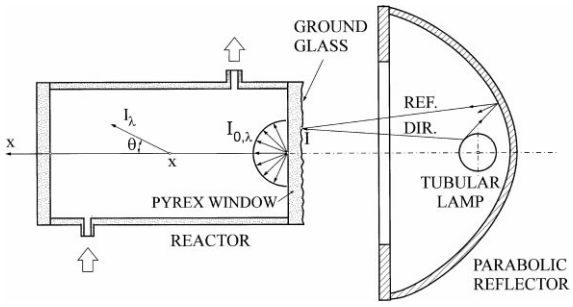

Fig. 11. The unidimensional photocatalytic reactor. Adapted from [2,14].

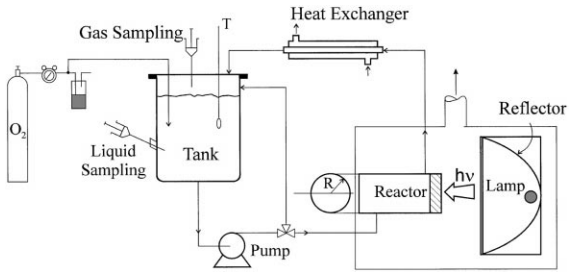

Fig. 12. Experimental set-up for photocatalytic reaction kinetics. Adapted from [17,18].

path (L_R) sufficiently large to ensure that no radiation is arriving at the flat plate facing the window of radiation entrance. With a radius of 5.2 cm and a length of 10 cm, the reactor volume is 212.4 cm^3. Illuminating the reactor through the ground glass face produces diffuse irradiation inside (the irradiation boundary condition) which greatly simplifies the radiation model.

2. A tubular UV lamp of well-known characteristics: output power, radiation spectral distribution of its output energy and geometrical dimensions. It is a 360 W, UA3-UVIARC lamp, from GE. Its operation is continuously monitored with a W–A–V meter. Any other geometrically similar, tubular lamp could be used in this equipment.
3. A cylindrical reflector of parabolic cross-section with well-known reflecting properties (Alzak® from Alcoa) and well-defined geometrical dimensions. The lamp is placed at its focal axis and the distance from the reflector to the reactor is precisely measured and controlled.

Under these conditions, emission by the irradiating system onto the reactor window can be rigorously modeled. This model will provide the necessary boundary condition for integrating the RTE.

The reacting system was operated inside the loop of a batch recycling arrangement (Fig. 12) with provisions for: (1) a storage tank made of glass with a volume of 2100 cm^3, (2) an all glass and Teflon recirculating pump with high flowrate capacity, (3) a device for the exact positioning of the reactor and the reflector (with the lamp), (4) a shutter to isolate the lamp from the reactor in order to reach stable operation before starting each run, (5) a temperature control system, (6) a continuous feed for oxygen, (7) two sampling ports in the tank: for the headspace and for the liquid, (8) a stirring device, and (9) an exhausting system. All connecting lines were made of glass. For other details concerning this reactor the reader can see Cabrera et al. [17–19].

A laboratory reactor must be constructed in such a way that an exact analysis of the experimental results should be simplified as much as possible. This experimental device has four important features for its modeling: (1) the tank volume is significantly larger than the reactor volume, (2) the pump has a high flow rate, (3) irradiation at the inside side of the reactor windows is diffuse, and (4) no radiation arrives at the opposite face of the reactor plate. The first two characteristics

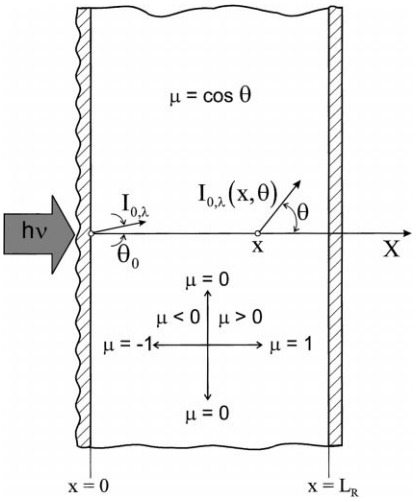

Fig. 13. Radiation field modeling of the unidimensional photocatalytic reactor. Adapted from [11].

simplify the mass balance and the other two have the same effect on the radiation balance.

As shown by Cabrera et al. [17] this reactor can be modeled with a one-dimensional — one-directional radiation model and rather simple boundary conditions for the RTE (Fig. 13). Hence, with azimuthal symmetry derived from the diffuse emission at x=0:

$$\mu\frac{\partial I_\lambda(x,\mu)}{\partial x}+(\kappa_\lambda+\sigma_\lambda)I_\lambda(x,\mu)=\frac{\sigma_\lambda}{2}\int_{\mu'=-1}^{1}I_\lambda(x,\mu')p(\mu,\mu')\,\mathrm{d}\mu' \quad (32)$$

with $\mu=\cos\theta$ and the following boundary conditions:

$$I_\lambda(0,\mu)=I_{0,\lambda},\quad \mu>0 \quad (33a)$$

$$I_\lambda(L_R,\mu)=0,\quad \mu<0 \quad (33b)$$

Diffuse radiation permit to consider incoming intensities independent of direction. Eq. (33b) profits by the fact that no radiation is arriving at x=L_R. At this point we need the value of $I_{0,\lambda}$. It can be obtained by two different approaches:

1. With an emission model for the tubular lamp and the parabolic reflector [6–8]. This model, with no adjustable parameters, permits to calculate radiation intensities at any point on the reactor window if the lamp and reflector characteristics and geometric dimensions are known. It takes into account both direct and reflected radiation. These intensities can then be transformed into fluxes (Eq. (5)) and both contributions added at x=0−e (with e being the wall thickness). It was found that, with the adopted arrangement, radiation fluxes were fairly uniform on the surface of radiation entrance. They were, however, averaged over the surface of the window, affected by the experimentally measured wall transmission coefficient and transformed into direction independent intensities according to

$$\langle q_{T,\lambda}(r,\beta)\rangle_{A_R}=\frac{4}{\pi r_R^2}\int_0^{r_R}r\,\mathrm{d}r\int_0^{\pi/2}\mathrm{d}\beta[q_{D,\lambda}(r,\beta)+q_{Rf,\lambda}(r,\beta)] \quad (34)$$

$$I_{0,\lambda}=\frac{1}{\pi}Y_{R,\lambda}\langle q_{T,\lambda}(r,\beta)\rangle_{A_R} \quad (35)$$

2. The boundary condition can also be obtained with homogeneous actinometry inside the reactor.

We have used the first method and verified the results with the second, employing the well-known uranyl oxalate actinometer.

Eq. (32) with BCs (33a) and (33b) was solved with the discrete ordinate method. At this point, absorption and scattering coefficients, as well as the phase function for scattering must be available. Solution in terms of intensities can be immediately used to calculate local values of the LVREA. Optical properties were assumed constant (stable catalyst) and consequently, since the organic compound is transparent (300<λ<400 nm), the κ_λ and σ_λ values are only a function of position. For the one-dimensional model it means that for calculating the values of e^a only the x coordinate and the catalyst concentration must be taken into account.

5.5. Interpretation of the heterogeneous reaction rate (the laboratory reactor mass balance model)

At this point we would like to relate the reaction rate per particle (Eq. (20)) with the value that can be experimentally measured in the laboratory reactor. With the results of the previous section, the rate of electron–hole generation can be calculated as a function of x. The time evolution of the pollutant concentration can be obtained from a mass balance.

Let us schematically consider a batch reacting system made of: (1) a flat plate reactor, (2) a storage tank, and (3) a high flow rate recirculating pump (Fig. 14). Similar systems are frequently employed in photocatalysis; we have chosen this experimental set-up to illustrate the proposed approach, but concepts can equally be extended to any other form of reactor operation.

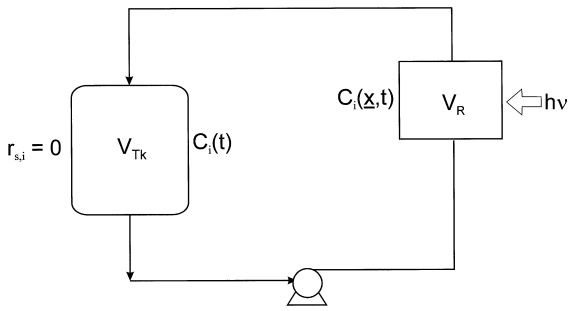

Fig. 14. Mass balance in the recycling system.

The following experimental conditions must be fulfilled:

1. The tank volume must be larger than the reactor volume. A safe relationship would be about 10 times larger.
2. The recirculating flow rate must be very high in order to accomplish:
   - Very good mixing.
   - Very low conversion per pass in the reactor.
   - Uniform concentration of the catalyst.
3. Oxygen must be always in excess with respect to the stoichiometric demand (because the adopted kinetic scheme does not account for oxygen concentration effects).
4. The volume of the connecting lines and that of the pump should be negligible with respect to the tank volume or they must be included in the said volume.
5. Isothermal conditions must be maintained.
6. Fouling of the reactor wall for radiation entrance should be minimized or accounted for.
7. The lamp operation must be stable.
8. Steady state conditions for pollutant adsorption, flow rates and temperatures must be reached before starting a run.

Starting from a local mass balance for a component i in the liquid phase [18] and using the methodology described by Cabrera et al. [19], the following mathematical expression can be derived:

$$\varepsilon_{\mathrm{L}} \frac{V_{\mathrm{R}}}{V_{\mathrm{Tk}}} \frac{\mathrm{d}}{\mathrm{d}t} \left\langle C_i(\underline{x}, t) \right\rangle_{V_{\mathrm{L,R}}} + \varepsilon_{\mathrm{L}} \left. \frac{\mathrm{d}C_i(t)}{\mathrm{d}t} \right|_{\mathrm{Tk}} = \frac{V_{\mathrm{R}}}{V_{\mathrm{Tk}}} a_V \left\langle r_{\mathrm{S},i}(\underline{x}, t) \right\rangle_{A_{\mathrm{Sol,R}}} \tag{36}$$

where ε_{L} is the liquid hold-up that is uniform throughout, a_V the catalytic surface area per unit suspension volume and $r_{\mathrm{S},i}$ the heterogeneous reaction rate (see Fig. 15).

Since $V_{\mathrm{R}}/V_{\mathrm{Tk}} < 1$ (from our design specifications) and the conversion per pass is very small (again a design condition) we finally get

$$\varepsilon_{\mathrm{L}} \left. \frac{\mathrm{d}C_i(t)}{\mathrm{d}t} \right|_{\mathrm{Tk}} = \frac{V_{\mathrm{R}}}{V_{\mathrm{Tk}}} a_V \left\langle r_{\mathrm{S},i}(\underline{x}, t) \right\rangle_{A_{\mathrm{Sol,R}}} \tag{37}$$

Since

$$a_V = S_{\mathrm{g}} C_{\mathrm{mp}} \ \text{ and } \ r_{\mathrm{S},i}(\underline{x}, t) = \frac{r_{\mathrm{P}}(\underline{x}, t)}{a_{\mathrm{S}}} \tag{38}$$

the reaction rate per unit suspension volume results:

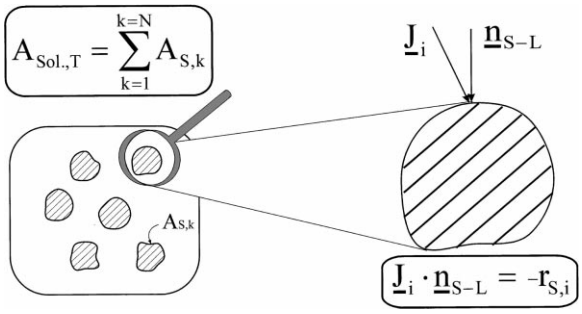

Fig. 15. Interpretation of the heterogeneous reaction rate for the mass balance in the liquid phase.

$$r_i|_{\mathrm{Susp}} = r_{\mathrm{S},i} a_V = \alpha_1^* C_{\mathrm{mp}} S_{\mathrm{g}} \frac{\alpha_{3,i}^*[R_i]}{1 + E(R_i, R_j)} \times \left\{ -\frac{E(R_i, R_j)}{1 + E(R_i, R_j)} + \left(\left\{ \frac{E(R_i, R_j)}{1 + E(R_i, R_j)} \right\}^2 + \frac{\alpha_2^*}{C_{\mathrm{mp}}} \int_{\lambda_1}^{\lambda_2} \mathrm{d}\lambda \, e_\lambda^{\mathrm{a}} \left[(C_{\mathrm{mp}}), \underline{x} \right] \right)^{1/2} \right\} \tag{39}$$

However, experimental results do not render local values of the reaction rate. In Eq. (39), concentrations are uniform (for the assumed good mixing conditions inside the reactor and the tank) but e^{a} is still a function of position. Consequently, in Eq. (39) we need the total catalytic surface area averaged reaction rate. For the unidimensional model, it can be shown [17] that when

1. The cross-sectional area corresponding to the irradiated flat plate reactor is constant (a design condition).
2. The catalyst concentration is uniform in the whole reactor volume (an established operating condition)

$$\left\langle r_{\mathrm{s},i}|_{\mathrm{Susp}} \right\rangle_{A_{\mathrm{Sol,R}}} = \left\langle r_{\mathrm{s},i}|_{\mathrm{Susp}} \right\rangle_{L_{\mathrm{R}}} \tag{40}$$

Then, for the unidimensional model:

$$\langle r_{\mathrm{S},i}(x, t) \rangle_{L_{\mathrm{R}}} = \frac{1}{L_{\mathrm{R}}} \int_0^{L_{\mathrm{R}}} \mathrm{d}x \, r_{\mathrm{S},i}(x, t) \tag{41}$$

Finally, the changes in concentration in the tank volume (where sampling is to be made) are related to the reaction rate per unit surface area of catalyst inside the photoreactor according to

$$\varepsilon_{\mathrm{L}}\frac{\mathrm{d}C_i(t)}{\mathrm{d}t} = -\frac{V_{\mathrm{R}}}{V_{\mathrm{Tk}}}\alpha_1^* C_{\mathrm{mp}} S_{\mathrm{g}} \left\{ \frac{\alpha_{3,i}^* C_i(t)}{1+\alpha_{3,i}^* C_i(t)} \right\} \times \frac{1}{L_{\mathrm{R}}}\int_0^{L_{\mathrm{R}}} \mathrm{d}x \left\{ \frac{\alpha_{3,i}^* C_i(t)}{1+\alpha_{3,i}^* C_i(t)} + \left(\left\{ \frac{\alpha_{3,i}^* C_i(t)}{1+\alpha_{3,i}^* C_i(t)} \right\}^2 + \frac{\alpha_2^*}{C_{\mathrm{mp}}} e^{\mathrm{a}}_{\Sigma\lambda}(x, C_{\mathrm{mp}}) \right)^{1/2} \right\} \quad (42)$$

where we have considered that only TCE is present. In Eq. (42):

$$\alpha_{3,i}^* = \frac{k_9 K_{3,i}[\mathrm{site}] a_{\mathrm{S}}}{k_{6-}} + \frac{k_{10} K_{3,i}[\mathrm{site}]}{k_{6-} K_4 [\mathrm{Ti}^{\mathrm{IV}}]} + \frac{k_{11}}{k_{6-}} + \frac{k_{12}}{k_{6-} K_4 [\mathrm{Ti}^{\mathrm{IV}}] a_{\mathrm{S}}} \quad (43)$$

$$e^{\mathrm{a}}_{\Sigma\lambda}(x, C_{\mathrm{mp}}) = \int_{300\,\mathrm{nm}}^{400\,\mathrm{nm}} \mathrm{d}\lambda \left[\kappa_\lambda^*(C_{\mathrm{mp}})\right] \times \int_{-1}^{1} I_\lambda(x, \mu, C_{\mathrm{mp}})\,\mathrm{d}\mu \quad (44)$$

Eqs. (42) and (44) indicates that the dependence of the reaction rate with respect to the catalyst concentration is very complex, even from the radiation point of view. Obviously, for a catalytic reaction the surface area for adsorption will also be very important, thus incorporating additional components to the catalyst loading effect. When only one species is present, Eq. (42) can be integrated with the initial condition:

$$t = 0 \rightarrow C_i = C_i^0 \quad (45)$$

Integration of Eq. (42) is possible because we know: (1) the boundary condition for the irradiated surface of the reactor, (2) the properties that are needed to calculate the radiation field inside the flat plate reactor and the method to integrate the RTE in the experimental reactor, (3) point values of the LVREA and the subsequent reactor volume averaged reaction rates (in principle, they are averages over the total surface of the catalytic particles), (4) that for the low catalyst concentration usually employed, the liquid hold-up is practically equal to one, (5) the reactor volume and the tank volume, and (6) the catalyst loading and the catalyst surface area.

Then, predictions of the concentration vs. time relationships can be compared with experiments, which were performed at different catalyst and TCE initial concentrations. With a non-linear parameter estimator and an optimization program, the three unknown kinetic constants can be obtained.

The final outcome is a kinetic model with three known constants that can be used for scaling-up purposes because this result is independent of the employed lamp and the particular reactor configuration that was used to get it. Several special considerations must be made to this statement: (1) If the activation step quantum yield is a strong function of wavelength, the average values employed in Eq. (29) could loose part of its validity. Then, the spectral distribution of the employed lamp output may have some effect on the parameters' result. (2) The catalyst has been assumed stable (no aging or poisoning) and fouling effects have not been considered. Employing some varieties of titanium dioxide catalyst fouling can be drastically minimized but this is not the case of the one most commonly used (Degussa P 25). (3) A single component has been used in the kinetic model and consequently intermediate reaction products effects have not been considered. Some of them could have a negative effect in the catalyst surface area (active sites) availability. (4) No effects of oxygen or impurities concentrations have been included in the model. (5) No temperature effects were included in the model. (6) In our particular case, we have worked with a restricted range of TCE concentrations and always starting with the pH of the pure water (plus catalyst) employed in our runs (pH 6.8). This pH decreases along the reaction to a value close to 4. Table 3 and Fig. 16 illustrate some of the results.

Table 3
Numerical values for the kinetic constants

Kinetic constant	α_1^*	α_2^*	$\alpha_{3,i}^*$
Units	$\mathrm{mol\,cm^{-2}\,s^{-1}}$	$\mathrm{g\,s\,Einstein^{-1}}$	$\mathrm{cm^3\,mol^{-1}}$
Values	2.46×10^{-14}	1.57×10^{11}	6.42×10^{6}

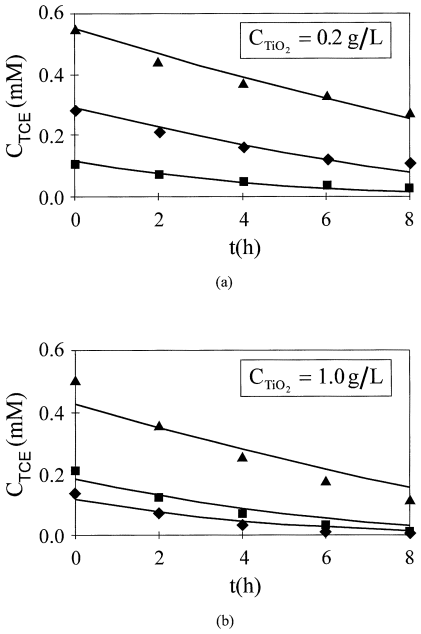

Fig. 16. TCE reaction kinetic model. Comparison of experimental data and model predictions. Reproduced from [19]. Copyright 1997 with permission from Academic Press.

6. A flat plate reactor

A flat plate configuration is a good example to illustrate the distinctive characteristic of one photocatalytic reactor design. The following topics will be reviewed:
1. Motivation.
2. The reactor radiation model.
3. The boundary conditions.
4. The experimental verification.
5. The field of radiation absorption rates.
6. The radiation collection efficiency.

6.1. Motivation

In a recent publication, Brandi et al. [20] made a rigorous and detailed analysis of the collection efficiencies of two types of solar reactors: (1) a flat plate, and (2) a parabolic trough with a cylindrical reaction tube. The basis for comparison was that the surface area of the flat plate reactor ($W\times l$) be equal to the aperture area of the parabolic collector ($W\times l$). The cylindrical reactor diameter was D and the distance from the reactor center to the parabola surface b. The particular condition when $D=W/\pi$ represents the case when the cylindrical surface area of the reactor will be equal to the surface area of the flat plate reactor.

For the flat plate reactor we considered: (1) direct radiation with an irradiating angle from the sun disc equal to $2\theta_S=0.54^\circ$ and (2) diffuse radiation (180°). For the parabolic trough reactor we considered: (1) direct radiation ($2\theta_S=0.54^\circ$) to the reactor tube, (2) diffuse radiation to the reactor tube, (3) direct radiation to the reflector ($2\theta_S=0.54^\circ$) that was then reflected to the reactor, and (4) diffuse radiation to the reflector that was also reflected to the reactor.

The specific intensities calculated by the model can be transformed into radiation fluxes. The two results for the flat plate are added and then averaged over the flat surface of the rectangular reactor [$A_{Plate}=W\times l$]. Similarly, the four values for the parabolic trough are added and averaged over the tubular area of the cylindrical reactor [$A_{Tube}=(\pi D)\times l$]. The model used one parameter and two variables:
1. The reflectivity of the parabolic surface.
2. The ratio of direct to diffuse solar radiation fluxes that is a function of the wavelength and the zenith angle:

$$\Lambda_\lambda = \frac{q_\lambda^{DIR}}{q_\lambda^{DIFF}} \tag{46}$$

3. The geometric concentration factor:

$$C_A = \frac{A_{Refl}}{A_{Tube}} = \frac{A_{Plate}}{A_{Tube}} = \frac{W}{D\pi} \tag{47}$$

Then, the energy collection efficiency can be defined as

$$\eta_E = \frac{E_{Tube}^{Total}}{E_{Plate}^{Total}} = \frac{D\pi}{W}\frac{\langle q_{Tube}^{Tot}(\beta,\Lambda)\rangle_{A_{Tub}}}{\langle q_{Plate}^{Tot}(\Lambda)\rangle_{A_{Pla}}} = \frac{\eta_q}{C_A} \tag{48}$$

If we assume that the reaction rate is proportional to the nth power of the LVREA and that back-scattering fluxes from the reactor surfaces can be accounted for in terms of a fraction ($X_{B\text{-}S}$) of the arriving photons, such that the fraction of absorbed photons will be $\gamma=1-X_{B\text{-}S}$ of those calculated from the arriving fluxes, then the apparent reaction efficiency can be calculated according to

$$\eta_{d,i} = \frac{\langle R_i\rangle_{V_{Tube}} V_{Tube}}{\langle R_i\rangle_{V_{Plate}} V_{Plate}} = \frac{K\,\langle (e^a)^n\rangle_{V_{Tube}} V_{Tube}}{K\,\langle (e^a)^n\rangle_{V_{Plate}} V_{Plate}} \tag{49}$$

1. Linear dependence (n=1):

$$\eta_{\mathrm{d},i} = \left(\frac{\gamma_{\mathrm{Tube}}}{\gamma_{\mathrm{Plate}}}\right)\left(\frac{E^{\mathrm{Total}}_{\mathrm{Tube}}}{E^{\mathrm{Total}}_{\mathrm{Plate}}}\right) = \omega\eta_{\mathrm{E}} \tag{50}$$

2. Square root dependence (n=0.5):

$$\eta_{\mathrm{d},i} = 1.3\left(\frac{\langle e^{\mathrm{a}}\rangle_{\mathrm{Tube}}}{\langle e^{\mathrm{a}}\rangle_{\mathrm{Plate}}}\right)^{0.5}\left(\frac{V_{\mathrm{Tube}}}{V_{\mathrm{Plate}}}\right) = 0.92\left(\frac{\omega\eta_{\mathrm{E}}}{C_{\mathrm{A}}}\right)^{0.5} \tag{51}$$

In Eq. (51), we have considered: $D/2$=h=1.0 cm and C_{mp}=1.0 g l^{-1}.

Figs. 17a and b present plots of these two efficiencies. The maximum hypothetical reaction efficiency of the parabolic trough reactor cannot be larger than 65% of that of the flat plate. It would reach this value only when: (1) the reflectivity of the reflector is 80% or larger, (2) direct radiation is 1.5 times larger than the diffuse one (a very optimistic upper limit for near UV radiation), (3) the cylindrical reactor (for W=1 m), has D=0.16 m, which, considering the high radiation absorption properties of titanium dioxide would be a very inefficient reactor, and (4) the reaction rate is first order with respect to the LVREA. The reason for this result is clear: parabolic concentrators are very ineffective in collecting diffuse solar radiation.

Considering at the same time that flat plate reactors are always cheaper than the parabolic collectors are clearly, the first one should be the preferred choice for photocatalytic reactions. With a cylindrical reactor, a much better efficiency can be achieved if compound parabolic reactors are used. However, in spite that the cylindrical tube can have some advantages from the hydrodynamic point of view, the reactor itself is by no means cheaper than the flat plate one. We concluded that studying flat plate systems for solar photocatalytic simulations is a good starting point for developing reactor design methods.

6.2. The reactor model

This model was developed to simulate with artificial lamps most of the features of a solar reactor [3,9]. Figs. 18 and 19 provide a representation of the custom-made reactor. It was made up of: (1) two 40 W Philips TLK 40/09N tubular lamps (L_{L}=56.5 cm) with continuous and superficial emission from 310 to 410 nm, with a pick at about 350 nm and a total output power each of 1.93×10^{-5} Einstein s^{-1}, (2) a reactor, made up of Tempax glass walls (thickness W_{t}=0.38 cm) having a width of 18.0 cm ($W_{\mathrm{R}}\ll L_{\mathrm{L}}$) and a reaction space thickness of 1.2 cm, and (3) two cylindrical reflectors of parabolic cross-section. The lamps, having a diameter of 3.8 cm were located at their focal axis. The dimensions of the reflectors were not pre-established for the reasons explained below.

It was desired to have an almost uniform radiation flux at the reactor surface of radiation entrance. We worked with three free design variables: (1) the distance from the reactor to the reflector, (2) the distance between the foci of the reflector parabolas, and (3) the parabola constant.

The radiation flux at any point on the surface of the reactor can be calculated from our previously developed models [2,4,6–8]. Emission from the lamp is

$$I_{\lambda,\mathrm{L}} = \frac{P_{\lambda,\mathrm{L}}}{2\pi^2 r_{\mathrm{L}} L_{\mathrm{L}}} \tag{52}$$

From geometric optics, intensities arriving at the external surface of the reactor can be calculated using somehow intricate trigonometric relationships, considering: (1) direct irradiation from the lamp and (2) indirect irradiation coming from the reflector:

$$I^{\mathrm{Dir}}_{\lambda}(x, y, z, \underline{\Omega}) = I^{\mathrm{Ideal}}_{\lambda,\mathrm{L}}\Im_1 \ \{\text{limiting angles defined by the directions of the rays coming from the whole lamp and arriving at point :}x, y = 0\} \tag{53}$$

The limiting angles of the function $\Im_1$ correspond to the visual solid angle required to see the lamp boundaries from the point of radiation reception (Fig. 19).

$$I^{\mathrm{Ref}}_{\lambda}(x, y, z, \underline{\Omega}) = I^{\mathrm{Ideal}}_{\lambda,\mathrm{L}}\Gamma_{\lambda,\mathrm{Rf}}\Im_2 \ \{\text{limiting angles defined by the directions of the reflected rays coming from the whole virtual image of the lamp and arriving at point :}x, y = 0\} \tag{54}$$

Similarly, the limiting angles of the function $\Im_2$ correspond to the visual solid angle required to see the virtual image of the lamp boundaries on the specular surface, from the point of radiation reception.

Once the intensities at each point are known, fluxes can be calculated according to Eq. (5) and then added up:

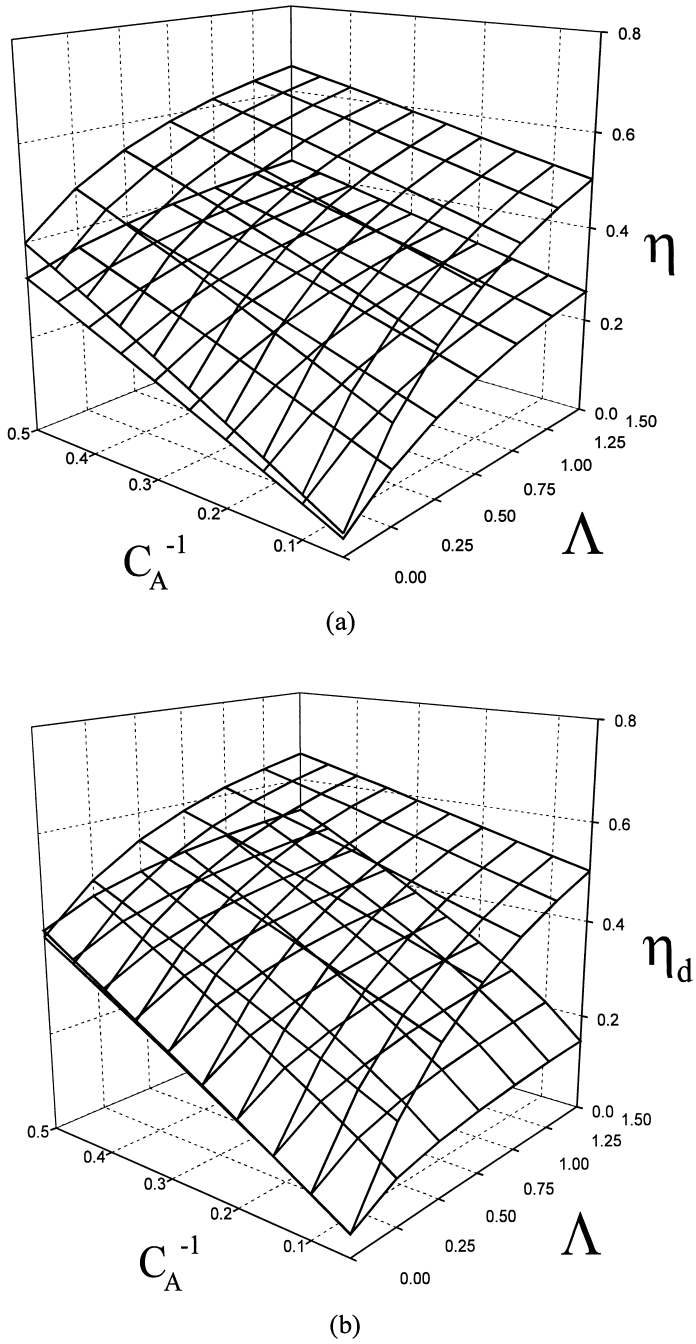

Fig. 17. Collection efficiencies of solar reactors. (a) Energy efficiencies; the upper surface is for an average reflection coefficient equal to 0.8 and the lower for 0.4; (b) Reaction efficiencies; the upper surface is for first order dependence and the lower for square root dependence. Reproduced from [20]. Copyright 1999 with permission from Science & Technology Integration.

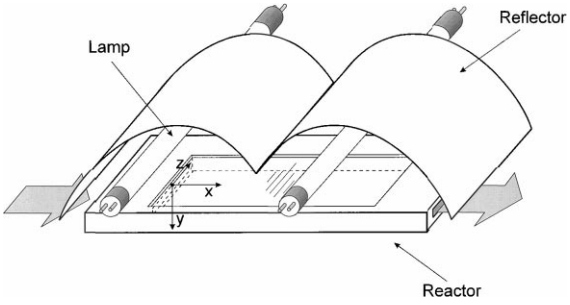

Fig. 18. Flat plate reactor configuration. Reproduced from [21]. Copyright 1998 with permission from Science & Technology Integration.

$$q_{\lambda,y}(x,\, y=0-W_t,\, z) = \left(q^{\mathrm{Dir}}_{\lambda,y}+q^{\mathrm{Ref}}_{\lambda,y}\right)_{\mathrm{System\ I}} + \left(q^{\mathrm{Dir}}_{\lambda,y}+q^{\mathrm{Ref}}_{\lambda,y}\right)_{\mathrm{System\ II}} \quad (55)$$

Then an optimization program was developed that produced the reflector dimensions and distances that are necessary to have an almost uniform flux (within 5% deviation) at the position $y=0-W_t$.

The result provided the following data: (1) distance $P_{R-Ref}=0.62$ cm, (2) distance $P_{F,A-F,B}=19.2$ cm, and (3) parabola constant $a=2.4$ cm. With these data, the following adoptions were made: (1) parabola height $H_P=9.6$ cm, (2) reflector length=54 cm, and (3) reactor height (for two reflectors) $L_R=34$ cm. With this arrangement, the arriving radiation field was almost independent of the z coordinate.

Since the radiation field distribution was almost independent of z, a two-dimensional (x,y) — two directional (θ,ϕ) model was proposed according to

$$\mu\frac{\partial I_\lambda(x,\, y,\, \underline{\Omega})}{\partial x}+\eta\frac{\partial I_\lambda(x,\, y,\, \underline{\Omega})}{\partial y} = -(\kappa_\lambda+\sigma_\lambda)I_\lambda(x,\, y,\, \underline{\Omega}) + \frac{\sigma_\lambda}{4\pi}\int_{4\pi} p(\underline{\Omega}'\rightarrow\underline{\Omega})I_\lambda(x,\, y,\, \underline{\Omega}')\,\mathrm{d}\Omega' \quad (56)$$

$$\mu=\cos\theta \ \text{ and } \ \eta=\sin\theta\cos\phi \quad (57)$$

6.3. Boundary conditions

This model calls for four boundary conditions: (1) at $y=0$ for every x, (2) at $y=H_R$ for every x, (3) at $x=0$ for every y, and (4) at $x=L_R$ for every y. At $y=0$ we must take into account reflections at both interfaces ($y=0$ and $y=0-W_t$), internal absorption by the glass and back-scattering from the suspension that can also be reflected by the liquid–solid interface (Fig. 20). A similar phenomenon is found at $y=H_R$. The final equations are

$$I_{04,\lambda}(\underline{x},\, \underline{\Omega}) = Y_{W,\lambda}(\underline{\Omega})I_{i1,\lambda}(\underline{x},\, \underline{\Omega}) + \Gamma_{SGA,\lambda}(\underline{\Omega})I_{i4,\lambda}(\underline{x},\, \underline{\Omega}) \quad (58)$$

$$I_{05,\lambda}(\underline{x},\, \underline{\Omega}) = \Gamma_{SGA,\lambda}(\underline{\Omega})I_{i5,\lambda}(\underline{x},\, \underline{\Omega}) \quad (59)$$

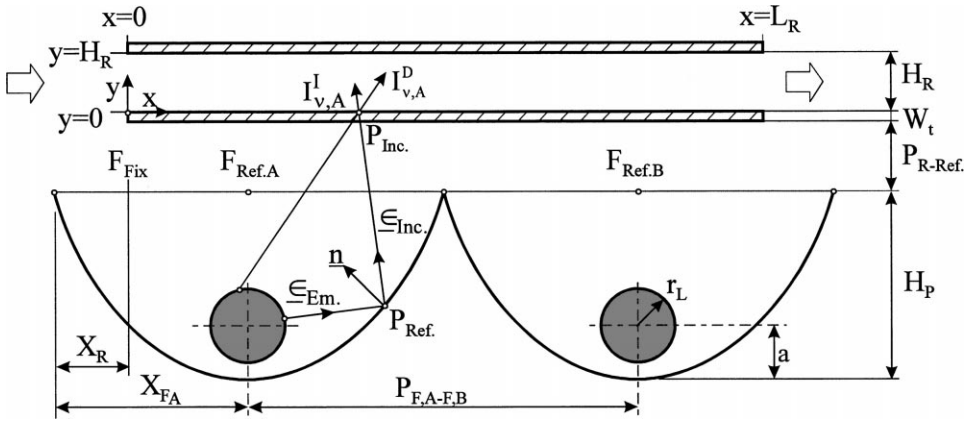

Fig. 19. Geometry for the flat plate photocatalytic reactor model. Reproduced from [21]. Copyright 1998 with permission from Science & Technology Integration.

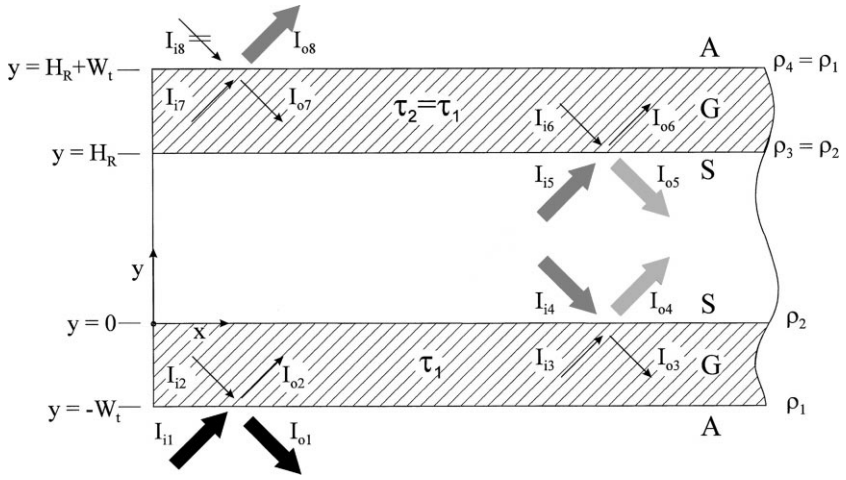

Fig. 20. The boundary conditions for the flat plate photocatalytic reactor model. Reproduced from [9]. Copyright 1999 with permission from Elsevier Science.

with

$$\Gamma_{\mathrm{AGS},\lambda}(\underline{\Omega}) = \frac{\rho_2 - 2\rho_1\rho_2\tau_1^2 + \rho_1\tau_1^2}{1 - \rho_1\rho_2\tau_1^2} \tag{60}$$

$$\Gamma_{\mathrm{SGA},\lambda}(\underline{\Omega}) = \frac{\rho_1 - 2\rho_1\rho_2\tau_1^2 + \rho_2\tau_1^2}{1 - \rho_1\rho_2\tau_1^2} \tag{61}$$

$$\mathrm{Y}_{\mathrm{W},\lambda}(\underline{\Omega}) = \frac{(1-\rho_2)(1-\rho_1)\tau_1}{1 - \rho_1\rho_2\tau_1^2} \tag{62}$$

All reflectivities can be calculated according the Fresnel and Snell equations [10]. Boundary conditions at x=0 and x=L_{R} were calculated assuming that no radiation is coming in from these directions:

$$I_\lambda(x = 0, y, \underline{\Omega} = \underline{\Omega}_{\mathrm{in}}) = I_\lambda(x = L_{\mathrm{R}}, y, \underline{\Omega} = \underline{\Omega}_{\mathrm{in}}) = 0 \tag{63}$$

Notice that since $I_{\mathrm{i}4,\lambda}$ and $I_{\mathrm{i}5,\lambda}$ are not known before hand, iteration with the solution of Eq. (56) will be necessary. The problem was solved with the DOM and the solution provided the distribution of intensities as a function of (1) position (x,y), (2) direction (θ,ϕ), and (3) wavelength.

6.4. Experimental verification

Direct experimental verification of the radiation field distribution with a radiation detector is very difficult to access without introducing a significant distortion of the measured variable. An indirect, but equally precise method can be devised if one measure fluxes coming out of the reactor from both faces. Experimental determination of back-scattering and forwardly transmitted fluxes, having the suspension of titanium dioxide flowing through the reactor in a continuos manner as part of a batch recycling system were conducted.

In the same way that boundary conditions (58) and (59) were calculated, one can also evaluate the following intensities (Fig. 20):

$$I_{01,\lambda}(\underline{\mathrm{x}}, \underline{\Omega}) = \Gamma_{\mathrm{AGS},\lambda}(\underline{\Omega}) I_{i1,\lambda}(\underline{\mathrm{x}}, \underline{\Omega}) + Y_{\mathrm{W},\lambda}(\underline{\Omega}) I_{i4,\lambda}(\underline{\mathrm{x}}, \underline{\Omega}) \tag{64}$$

$$I_{08,\lambda}(\underline{\mathrm{x}}, \underline{\Omega}) = Y_{\mathrm{W},\lambda}(\underline{\Omega}) I_{i5,\lambda}(\underline{\mathrm{x}}, \underline{\Omega}) \tag{65}$$

From Eqs. (64) and (65) the net fluxes in the forward and the backward directions can be predicted and compared with experimental measurements. These verifications can be performed with precisely calibrated UV sensors. Great care was required for these calibrations because: (1) we are using polychromatic radiation, (2) the view angle of the different employed sensors must be carefully measured, and (3) not always the sensor can be placed in direct contact with the outgoing flux because it could produce a distortion of the radiation field that is being measured (Fig. 21). Details can be found in Brandi et al. [9].

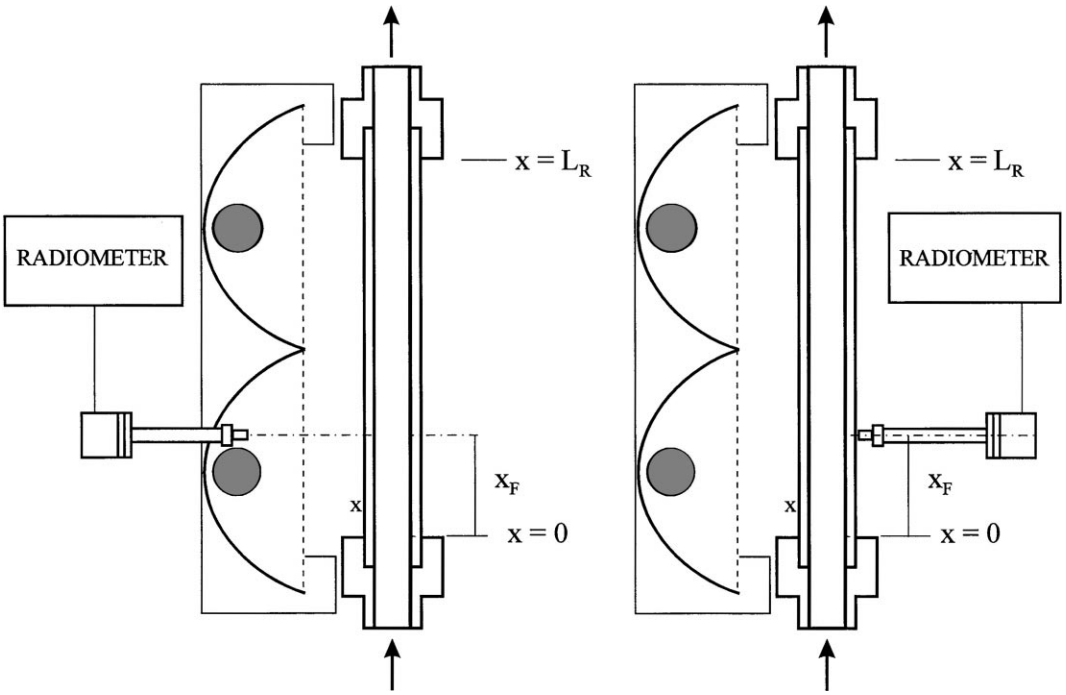

Fig. 21. Experimental verification of the radiation field predictions from the flat plate photocatalytic reactor model. Left: measurement of back scattering; right: measurement of forward scattering. Adapted from [9,21].

At the same time, these types of measurements can be used to decide upon the best phase function for scattering, particularly when prediction and measurement of back scattering are part of the experimental program. For measuring forwardly transmitted fluxes not too high concentrations of titanium dioxide can be used because considering the high absorption properties of titanium dioxide experimental measurements could be meaningless. Conversely, for measuring back-scattering, intermediate to high solid concentrations will provide the best experimental conditions.

Predictions can be calculated according to

1. Transmitted radiation fluxes at $y=H_R+W_t$:

$$q_n(x, y = H_R + W_t) = \int_{\lambda_{min}}^{\lambda_{max}} \int_{2\pi} I_{08}(x, y = H_R + W_t, \underline{\Omega})\underline{\Omega} \cdot \underline{n}\, d\Omega\, d\lambda \quad (66)$$

2. Radiation fluxes due to back-scattering at $y=0-W_t$:

$$q_n(x, y = 0 - W_t) = \int_{\lambda_{min}}^{\lambda_{max}} \int_{2\pi} I_{01}(x, y = 0 - W_t, \underline{\Omega})\underline{\Omega} \cdot \underline{n}\, d\Omega\, d\lambda \quad (67)$$

Theoretical values and experiments were made employing: (1) Aldrich and Degussa P 25 catalysts and (2) the diffuse and the isotropic phase function for the scattering model.

It was additionally found that using Aldrich titanium dioxide fouling of the reactor walls was not important. Conversely, employing Degussa P 25, the solid sticks significantly against the reactor walls. A fouling factor was then defined that was obtained with spectrophotometric measurements carried out under the same operating conditions than the ones used in the experimental reactor.

For different catalyst concentrations, predicted x-averaged radiation fluxes were also compared with experiments, according to

$$\langle q_n(x, y = H_R + W_t)\rangle_x = \frac{1}{L_R}\int_0^{L_R} q_n(x, y = H_R + W_t)\,dx \quad (68)$$

$$\langle q_n(x, y = 0 - W_t)\rangle_x = \frac{1}{L_R}\int_0^{L_R} q_n(x, y = 0 - W_t)\,dx \quad (69)$$

Fig. 22 (forward fluxes at different *x*-positions), Fig. 23 (forward fluxes with the two different phase functions) and Fig. 24 (backward fluxes with two different phase functions) show the results. It can be seen that except for the case of backward fluxes with low concentrations of Degussa P 25, employing the isotropic phase function, agreement was very good (errors, leaving aside the above-mentioned exception were never larger than 12%). It should be noted that in no case, experimentally adjusted parameters have been used; i.e., all these computations are ab initio.

From these results it was also concluded that the isotropic phase function is the best model for representing scattering by titanium dioxide suspensions. This result also completed the information required by the double loop iteration procedure for computing absorption and scattering coefficients.

6.5. Field of radiation absorption rates

Having confirmed that the developed model provides a reasonable representation of the radiation field, we can now have a look at the property that was defined as the distinctive problem at the beginning of this review. For this reactor, the LVREA is calculated according to

$$e^a_{\Sigma\lambda}(x, y) = \int_{\lambda_{min}}^{\lambda_{max}} e^a_\lambda(x, y)\,d\lambda = \int_{\lambda_{min}}^{\lambda_{max}} \kappa_\lambda \int_{4\pi} I_\lambda(x, y, \underline{\Omega})\,d\Omega\,d\lambda \quad (70)$$

This is a point-valued function of position. The first important result that can be derived from Eq. (70) is provided by looking at variations along the most significant direction for changes in the radiation field properties. Thus, in order to see variations of the LVREA along the *y*-coordinate let us calculate a *x*-averaged VREA:

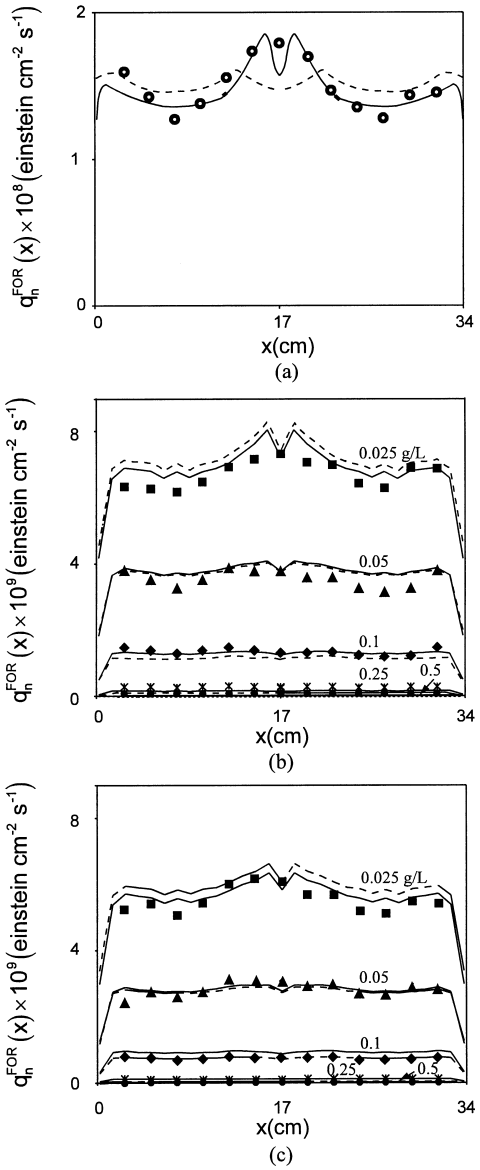

Fig. 22. Radiation fluxes in the flat-plate photocatalytic reactor. Model predictions vs. experimental data. (a) Values at $y=H_R+W_t$ for the empty reactor; (b) values at $y=H_R+W_t$ for the reactor with the Aldrich catalytic suspension; and (c) values at $y=H_R+W_t$ for the reactor with the Degussa P 25 catalytic suspension. Solid lines: diffuse phase function; dotted lines: isotropic phase function.

$$\left\langle e^a_{\Sigma\lambda}(x, y)\right\rangle_x = \frac{1}{L_R}\int_{x=0}^{x=L_R} e^a_{\Sigma\lambda}(x, y)\,dx \quad (71)$$

Fig. 25 portraits results for Degussa P 25 catalyst. The Aldrich variety provides similar plots. It can be

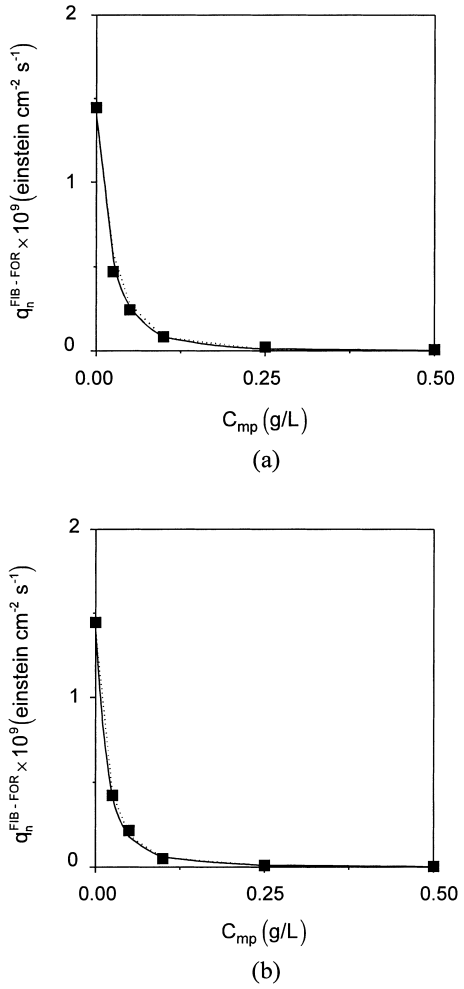

Fig. 23. Predictions vs. experimental values for forwardly transmitted, *x*-averaged radiation fluxes as a function of the catalyst loading in the flat plate photocatalytic reactor. (a) Aldrich, (b) Degussa P 25. Solid lines: diffuse reflection phase function; dotted lines: isotropic phase function.

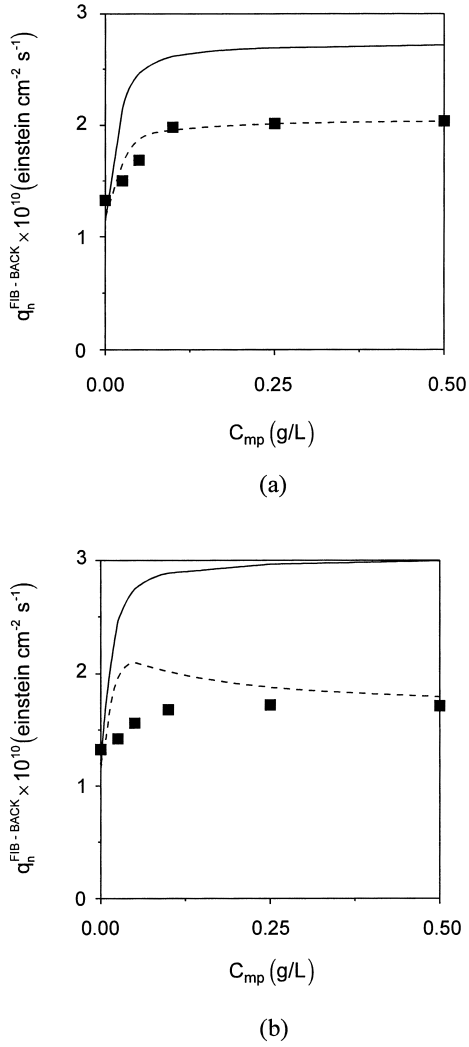

Fig. 24. Predictions vs. experimental values for back scattering, *x*-averaged radiation fluxes as a function of the catalyst loading in the flat plate photocatalytic reactor. (a) Aldrich, (b) Degussa P 25. Solid lines, diffuse reflection phase function; dotted lines, isotropic phase function. Reproduced from [9]. Copyright 1999 with permission from Elsevier Science.

seen that only for very low catalyst concentrations (well below the usually employed in photocatalysis) the radiation field is fairly uniform along the *y*-direction. For the more usual catalyst loadings (but still lower than the most frequently employed) the radiation field changes drastically along the *y*-direction. For this reactor, employing 0.5 g l^{-1} of Degussa P 25 catalyst and for y=0.5 cm the VREA is almost zero. This is true considering polychromatic radiation. Probably at some wavelengths longer than 350 nm, some light will be present. This means that, from the radiation absorption point of view, and only from this respect, concentrations higher than that should be not important. However, it must be pointed out that radiation absorption is not only the variable that affects photocatalytic reaction rates and, very frequently, catalyst concentrations greater than 2 g l^{-1} have been found to render the best results. Undoubtedly, prop-

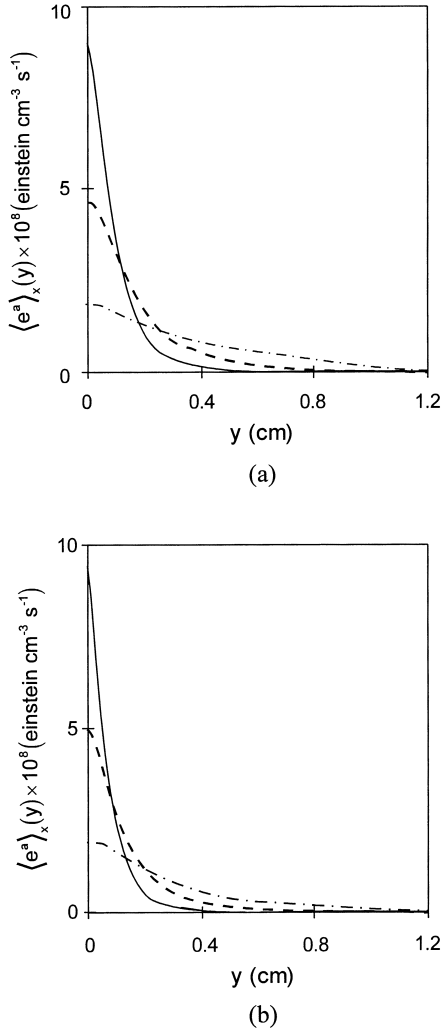

Fig. 25. *x*-averaged LVREA as a function of the penetration depth in the reactor. Catalyst concentration is the parameter. (a) Aldrich and (b) Degussa P 25. Solid lines: C_{mp}=0.5 g l^{-1}; Dashed lines: C_{mp}=0.25 g l^{-1}; Dot and dash lines: C_{mp}=0.1 g l^{-1}. Reproduced from [9]. Copyright 1999 with permission from Elsevier Science.

erties inherent to the catalytic activity other than the photon absorption rate have strong influence on the rates. These results, also indicate that the different regimes of dependence of the reaction kinetics with respect to the LVREA (linear, square root and intermediate transitions) can be found inside the same reactor when moving — in this case — from y=0 to y=H_R.

The second important property is the reactor volume-averaged LVREA:

$$\mathrm{VREA}|_{\Sigma\lambda} = \left\langle e^{a}_{\sum\lambda}(x,y)\right\rangle_{x,y} = \frac{1}{H_R L_R}\int_{x=0}^{x=L_R}\int_{y=0}^{y=H_R} e^{a}_{\Sigma\lambda}(x,y)\,dx\,dy \tag{72}$$

Fig. 26 gives a representation of these results. Again, from the radiation absorption point of view, around 0.5 g l^{-1} of catalyst loading, the photon absorption rate reaches a plateau and beyond that concentration no much improvement in the VREA can be achieved.

6.6. Radiation collection efficiency

For any reactor set-up, the photon collection efficiency can be defined by

$$\tau_A = \frac{\text{true absorbed energy in the reaction space}}{\text{energy entering through the reactor boundary}} \tag{73}$$

or

$$\tau_A = \frac{\int_{V_R}\langle e^{a}(x,y)\rangle_{V_R}\,dV}{\int_{A_{R,in}} q_n(x, y=0-W_t)\,dA} \tag{74}$$

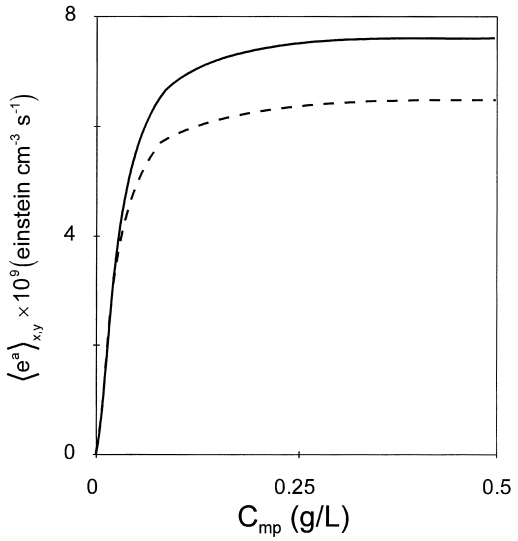

Fig. 26. Reactor volume averaged LVREA as a function of the catalyst loading. Solid line, Aldrich; broken line, Degussa P 25. Reproduced from [9]. Copyright 1999 with permission from Elsevier Science.

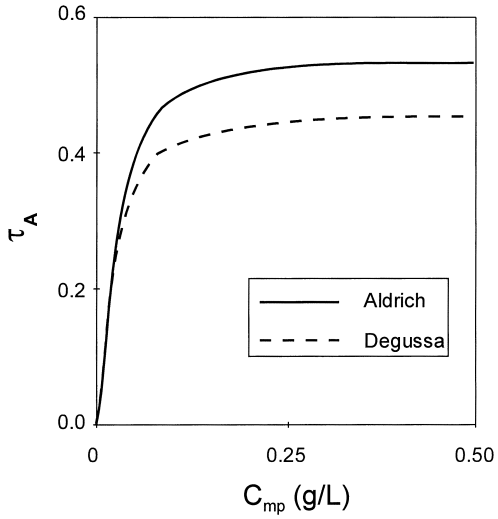

Fig. 27. Radiation absorption efficiencies of different catalysts as a function of the solid concentration.

This property tell us how many of the photons arriving to the reactor are absorbed inside its reaction volume. For Aldrich and Degussa P 25, these efficiencies are plotted in Fig. 27. Having Degussa P 25 a higher absorption coefficient this results may seem very surprising. However, this catalyst has also a very high scattering coefficient. For this particular reactor configuration, back scattering produces a very important loss of photons and is responsible for the better performance of the Aldrich catalyst.

7. Final remarks

Knowing the value of $e^a(x,y)$ and the reaction scheme (with the corresponding reaction kinetics) we can write the reaction rate at any point inside the reactor regardless of its size. A mass balance for the flat plate reactor, either operating in a continuous mode or as a part of a recycling system is a straightforward procedure. No thermal energy balance will normally be required because due to the usually low pollutant concentrations thermal effects from the reaction will be negligible. The mass balance will predict output concentrations of the pollutants coming out from the reactor. The same equations can be used to decide, for a fixed output concentration, the required reactor length. If we decide to maintain this reactor configuration, in order to satisfy the calculated reactor length we may add as many lamp-reflector systems as needed. However, the reaction kinetics (for any reactor shape) and the radiation distribution for a flat plate geometry (regardless the system of illumination) will be always valid. Needless is to say that the same equations can also be used to optimize any one of the reactor operating variables, e.g., catalyst concentration.

8. Conclusions

In the above sections we have been trying to show a method that could lead to an a priori design of photocatalytic reactors, employing only data from laboratory experiments and specially avoiding the use of experimentally adjustable design parameters. However, much work needs to be done to reach the final objective. This is particularly true for water environments where many additional variables affect the rates. Thus, obtaining intrinsic kinetics information for real wastewaters appears to be a formidable challenge.

Other reacting systems must be equally explored and much progress in reactors employing immobilized catalyst (to avoid solid particles separation costs) is urgently needed.

Regarding suspended solid photocatalytic reactors in liquid–solid systems only a few theoretically sounded and realistic design methods are available. They have been introduced in the scientific literature in the past few years. Unfortunately, reported large-scale applications seem to be at present time inexistent and medium size processes or pilot scale studies are also scarce.

Conversely, applications in gas–solid systems, particularly with immobilized catalysts, are growing very fast; even faster that the scientific understanding of the involved phenomena. Very high reaction rates have been observed in the gas phase and these results explain the difference.

For this reason the authors feel that paralleling more research efforts in developing reliable intrinsic kinetics and design methods for other reactor configurations and operations, applications in water environments ask desperately for much more efficient catalysts.

Acknowledgements

The financial support of Universidad Nacional del Litoral, CONICET (Argentina) and ANPCyT (FONCyT Program, Argentina) are gratefully acknowledged. A.E.C. wrote his contributions for this paper while being in Germany supported by the Alexander von Humboldt Foundation and kindly hosted by the ISFH (Hannover).

References

[1] G. Spadoni, E. Bandini, F. Santarelli, Chem. Eng. Sci. 33 (1978) 517.
[2] A.E. Cassano, C.A. Martín, R.J. Brandi, O.M. Alfano, Ind. Eng. Chem. Res. 34 (1995) 2155.
[3] R.J. Brandi, O.M. Alfano, A.E. Cassano, Chem. Eng. Sci. 51 (1996) 3169.
[4] H.A. Irazoqui, J. Cerdá, A.E. Cassano, AIChE J. 19 (1973) 460.
[5] J. Cerdá, H.A. Irazoqui, A.E. Cassano, AIChE J. 19 (1973) 963.
[6] O.M. Alfano, R.L. Romero, A.E. Cassano, Chem. Eng. Sci. 40 (1985) 2119.
[7] O.M. Alfano, R.L. Romero, A.E. Cassano, Chem. Eng. Sci. 41 (1986) 1155.
[8] O.M. Alfano, R.L. Romero, A.E. Cassano, Chem. Eng. Sci. 41 (1986) 1163.
[9] R.J. Brandi, O.M. Alfano, A.E. Cassano, Chem. Eng. Sci. 54 (1999) 2817.
[10] R. Siegel, J.R. Howell, Thermal Radiation Heat Transfer, 3rd Edition, Hemisphere, Bristol, PA, 1992.
[11] M.I. Cabrera, O.M. Alfano, A.E. Cassano, J. Phys. Chem. 100 (1996) 20043.
[12] J.J. Duderstadt, E.R. Martin, Transport Theory, Wiley, New York, 1979.
[13] R.L. Romero, O.M. Alfano, A.E. Cassano, Ind. Eng. Chem. Res. 36 (1997) 3094.
[14] O.M. Alfano, M.I. Cabrera, A.E. Cassano, J. Catal. 172 (1997) 370.
[15] M.N. Ozisik, Radiative Transfer and Interactions with Conduction and Convection, Wiley, New York, 1973.
[16] C.S. Turchi, D.F. Ollis, J. Catal. 122 (1990) 178.
[17] M.I. Cabrera, O.M. Alfano, A.E. Cassano, Ind. Eng. Chem. Res. 33 (1994) 3031.
[18] J.C. Slattery, Momentum, Energy, and Mass Transfer in Continua, McGraw-Hill, New York, 1978.
[19] M.I. Cabrera, A.C. Negro, O.M. Alfano, A.E. Cassano, J. Catal. 172 (1997) 380.
[20] R.J. Brandi, O.M. Alfano, A.E. Cassano, J. Adv. Oxid. Technol. 4 (1999) 76.
[21] R.J. Brandi, O.M. Alfano, A.E. Cassano, J. Adv. Oxid. Technol. 3 (1998) 213.
[22] M.I. Cabrera, O.M. Alfano, A.E. Cassano, Ind. Eng. Chem. Res. 34 (1995) 500–509.